Journal of Structural Geology 141 (2020) 104212

Contents lists available at ScienceDirect

Journal of Structural Geology

journal homepage: http://www.elsevier.com/locate/jsg

Connectivity and network development of carbonate-hosted fault damage zones from western Malta

Casey W. Nixon [a,*], Kari Nærland [a,1], Atle Rotevatn [a], Vilde Dimmen [a], David J. Sanderson [b], Thomas B. Kristensen [a,2]

[a] Department of Earth Science, University of Bergen, Allegaten 41, 5007, Bergen, Norway
[b] Ocean and Earth Sciences, University of Southampton, Southampton, SO14 3ZH, UK

ARTICLE INFO

Keywords:
Connectivity
Fault damage zone
Topology
Fracture network
Graph theory

ABSTRACT

Using outcrop-based examples, we investigate the topological and graph characteristics of various fault damage zones in carbonate rocks on Malta. The damage zone fracture networks are analysed as a series of nodes (isolated *I*-nodes; connected *Y/X*-nodes) and branches (*II*-, *IC*-, *CC*-branches), which may link to form connected components and fracture-bounded regions. We compare the metrics of the different nodes, branches, regions and components that make-up each damage zone fracture network, calculating parameters that assess their connectivity. Results identify distinct topological signatures and graph metrics for different tip-, relay- and splay-damage zones, providing a new classification that describes and quantifies their arrangement and connectivity. Placing the studied damage zones in a fault evolutionary model highlights topological pathways whereby tip-damage zones, dominated by *I*-nodes and *II*-branches, give way to relay-damage zones, dominated by *Y*-nodes and *CC*-branches. During this process, tree-like components link to form larger interconnected components with many regions. This systematically changes the graph metrics of the network increasing the number of branches and regions relative to nodes and components. The topological pathways and graph metrics provide important insights into how damages zones might develop as faults propagate, interact and link and could have implications when assessing their importance for fluid-flow.

1. Introduction

Fault damage zones represent the volume of deformed rock surrounding a fault as a result of fault initiation, propagation, interaction and slip accumulation (e.g. Cowie and Scholz, 1992; McGrath and Davison, 1995; Kim et al., 2004; Choi et al., 2016; Peacock et al., 2017). A variety of different fault damage zones have been identified and classified in the literature depending on their location relevant to the parent fault(s), including but not limited to: tip, wall, linkage, interaction and fault bend damage zones (i.e. Kim et al., 2004; Choi et al., 2016; Peacock et al., 2017). Such damage zones form due to local stress concentrations or perturbations along or between faults, often accommodating variations in the distribution of strain and displacement (e.g. Kim et al., 2000, 2001; Nixon et al., 2019). They commonly consist of numerous fractures (e.g. veins, joints, small faults, deformation bands, stylolites etc.) of different scales, types and orientations, forming networks that contribute to the overall deformation of the rock.

A detailed understanding of the development of the different structures within fault damage zones can provide valuable insights on processes of fault growth and development (Cowie and Shipton, 1998; Kim et al., 2003; Shipton and Cowie, 2003; Fossen et al., 2005; Childs et al., 2009; Faulkner et al., 2011) as well as earthquake initiation and rupture patterns (King, 1986; Sibson, 1989; Kim and Sanderson, 2008; Soliva et al., 2008; Choi et al., 2012; Johri et al., 2014; Perrin et al., 2016). Of particular economic significance is the control of fault damage on fluid flow and rock permeability in the upper crust (Caine et al., 1996; Shipton et al., 2002; Leckenby et al., 2005; Kim and Sanderson, 2010; Mitchell and Faulkner, 2012; Ogata et al., 2014; Dimmen et al., 2017, 2020). Thus damage zones can be crucial factors when exploring for water aquifers (e.g. Huyakorn et al., 1983), ore mineral deposits (e.g. Curewitz and Karson, 1997), hydrocarbon reservoirs (e.g. Gartrell et al., 2004; Fossen et al., 2005; Rotevatn et al., 2007) and storage sites for CO_2 (e.g. Shipton et al., 2004; Dockrill and Shipton, 2010).

A plethora of literature, therefore, exists on fault damage zones with studies mainly focusing on characterising damage zone architectures and

* Corresponding author.
E-mail address: casey.nixon@uib.no (C.W. Nixon).
[1] Now at: ConocoPhillips, Ekofiskvegen 35, 4056 Tananger, Norway.
[2] Now at: Statoil, Sandslivegen 90, 5254 Sandsli, Norway.

https://doi.org/10.1016/j.jsg.2020.104212
Received 9 March 2020; Received in revised form 15 September 2020; Accepted 2 October 2020
Available online 7 October 2020

geometries (e.g. McGrath and Davison, 1995; Kim et al., 2001, 2004; Berg and Skar, 2005; Johansen and Fossen, 2008; Gudmundsson et al., 2010; Rotevatn and Bastesen, 2014; Choi et al., 2016; Peacock et al., 2017), geometric dimensions of damage zones and subsequent scaling relationships with fault displacement/length (e.g. Hull, 1988; Knott et al., 1996; Vermilye and Scholz, 1998; Beach et al., 1999; Shipton and Cowie, 2001; Mitchell and Faulkner, 2009; Faulkner et al., 2011), fracture abundances and distributions within damage zones (e.g. Micarelli et al., 2003, 2006; Berg and Skar, 2005; Savage and Brodsky, 2011) and the effects of damage on physical rock properties such as permeability (e.g. Caine et al., 1996; Shipton et al., 2002; Mitchell and Faulkner, 2012). Less attention, however, has been given to characterising the arrangement (topology) and connectivity of the fractures within fault damage zones. This is important as fracture connectivity is crucial for assessing percolation potential and thus fluid flow through a rock body (Adler and Thovert, 1999; Manzocchi, 2002; Sanderson and Nixon, 2018). This is especially the case in low permeability rocks, such as the carbonate rocks used in this study, where permeability is often solely reliant on fractures and their connectivity (Faulkner et al., 2010).

The aim of this paper is to investigate the topological characteristics of different fault damage zones, with a focus on quantifying the development of fracture connectivity. The study applies a topological analysis based on graph theory (i.e. Sanderson et al., 2019) to examples of damage zones associated with metre-scale extensional faults observed in carbonate rocks along the western coast of Malta (Fig. 1). A topological analysis provides a description of the geometrical relationships between the fractures within a network and is essential for assessing fracture network connectivity (Jing and Stephansson, 1997; Sanderson and Nixon, 2015, 2018). The topological character of a fracture network is important as two fracture networks can have similar geometries (trace lengths, orientations and fracture intensities) but different topologies and thus connectivity, which could result in very different fluid flow properties (e.g. Sanderson and Nixon, 2015, 2018). Therefore, this study focuses on constraining the potential variations in topology and connectivity of fracture networks within different fault damage zones. We explore the differences and similarities between the different types of damage zone, producing a topology-based classification scheme that describes both the connectivity and complexity of their fracture networks. Finally, we extrapolate the results to discuss how fracture networks develop within damage zones by using the different studied examples, with varying degrees of structural complexity, as proxies for damage zone maturity.

2. Damage zone terminology

Numerous studies have proposed different classification and nomenclature schemes for describing fault damage zones. Kim et al. (2004) define *tip*, *wall* and *linkage* damage zones based on their location around subparallel segmented faults. Peacock et al. (2017) broaden this classification to include *interaction damage zones* around non-parallel and non-synchronous faults including *intersection* and *approaching* damage zones. Choi et al. (2016) use *along-fault*, *around-tip* and *cross-fault* damage, an approach that describes a damage zone based on the plane of observation and the damage zone position around an exposed fault. In this paper we follow the recommendation of Peacock et al. (2017) and use a prefix based on the damage zones' location in order to distinguish the three different types of studied damage zone (Fig. 2):

- *Tip-damage zones* refer to damage around the lateral tips of an extensional fault, observed in plan-view. The damage in these zones is related to increased stresses at the tips of faults as they grow and propagate (e.g. Cowie and Scholz, 1992; Vermilye and Scholz, 1998). These are the same as tip damage zones described by Kim et al. (2004) and could either be mixed mode or mode III tip damage according to the around-tip damage zone classification of Choi et al. (2016).
- *Relay-damage zones* refer to damage around geometrically or kinematically linked, synchronous, sub-parallel and overlapping extensional faults, observed in plan-view. These damage zones can be associated with different stages of fault segment linkage from relay ramp structures between soft-linked faults to fully breached relays of hard-linked faults. The damage in these zones is related to fault interaction often accommodating the transfer of strain or displacement between two fault segments (e.g. Peacock and Sanderson, 1991, 1994; Huggins et al., 1995). These damage zones are equivalent to along-fault linkage damage zones (Kim et al., 2004; Choi et al., 2016).
- *Splay-damage zones* represent damage associated with upward splaying or bifurcating, synthetic faults that are observed in cross-section. These may be cross-sectional views of either a relay-damage zone or a mode

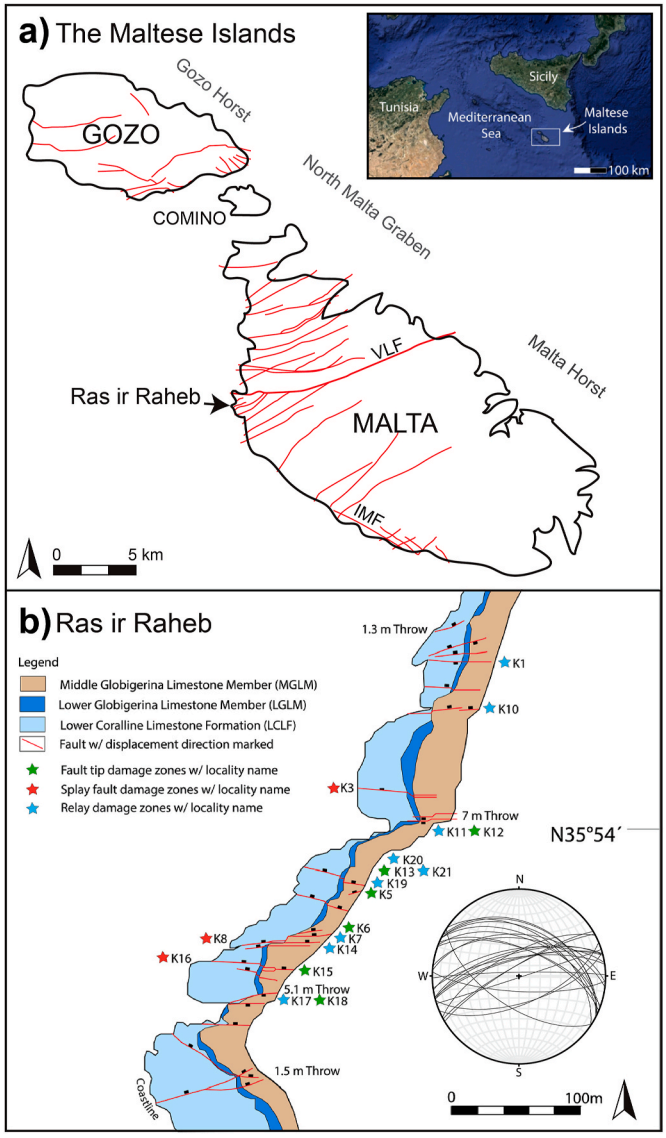

Fig. 1. a) Map of the Maltese Islands, showing the location of the largest faults in red (VLF = Victoria Lines Fault; IMF = Il Maghlaq Fault), and the location of the study area at the western coast of Malta (After Pedley et al., 1976; Michie et al., 2014; Dimmen et al., 2017). Inset image shows the regional location of the Maltese Islands within the Mediterranean Sea – attribution given to Google Earth (Data: SIO, NOAA, U.S. Navy, NGA, GEBCO; Image: Landsat/Copernicus). b) Map of the study area at Ras ir Raheb (After Michie et al., 2014). The stereoplot shows the trends of the normal faults found along the wave-cut platform on which the studied networks are situated (After Dimmen et al., 2017). The locations and names of the damage zones presented within this paper are marked by stars. (For interpretation of the references to colour in this figure legend, the reader is referred to the Web version of this article.)

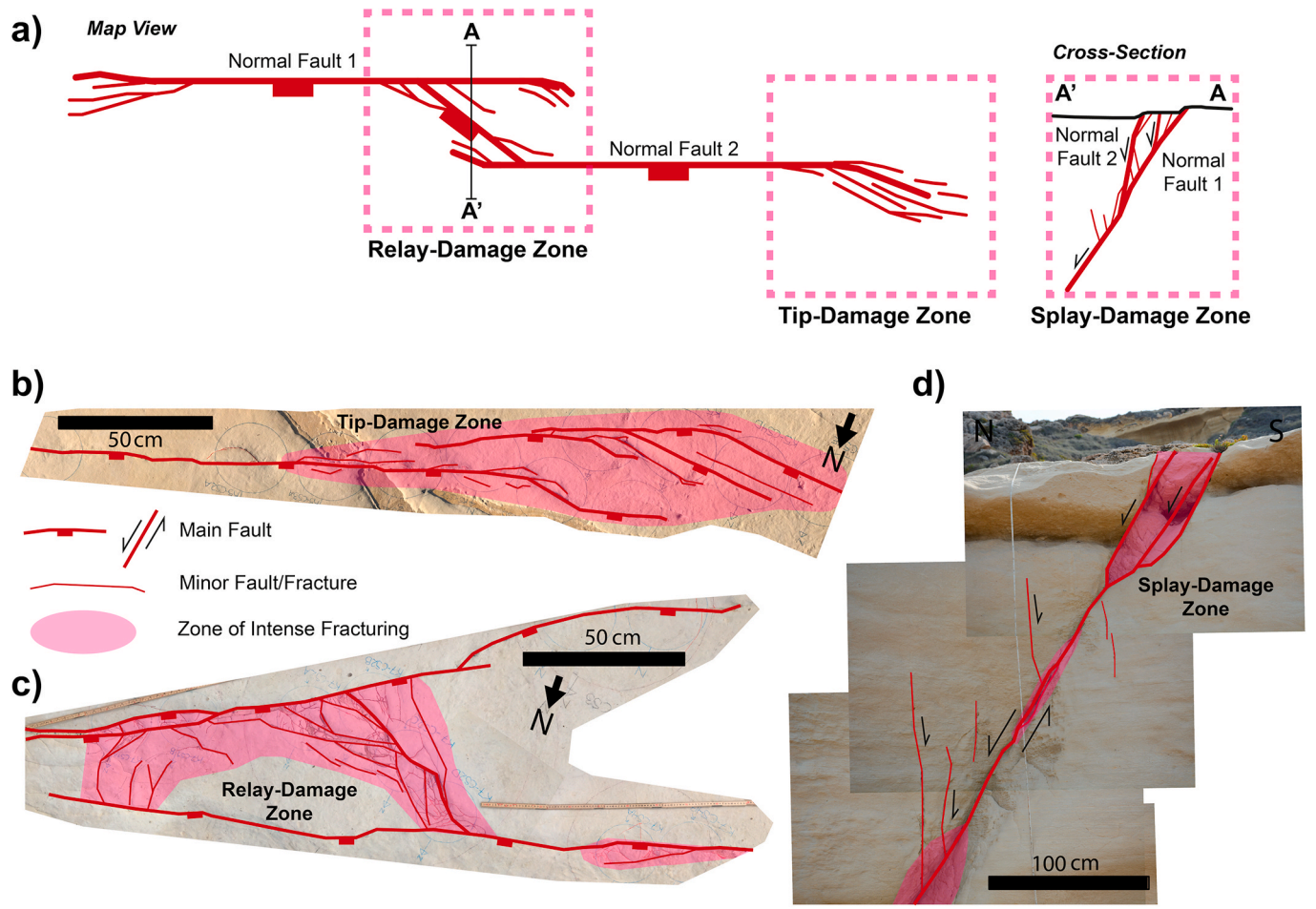

Fig. 2. a) Illustration of the different types of damage zone (tip-, relay-, splay-) according to where they are placed in relation to the overall geometry of the fault(s). These terms are used for normal fault damage zones in this study. b), c) and d) are interpreted photographs of localities K5, K7 and K3 respectively, showing field examples of the different types of damage zone. See Fig. 1b for locations of the three field examples.

III tip-damage zone, which could be considered as cross-fault damage or an around-tip damage, respectively (Choi et al., 2016).

These different damage zones are associated with local stresses during the propagation and linkage of faults as they grow and develop. We use several examples of each damage zone type to cover a range of structural complexities and as proxies for evolutionary stages of damage zone development during fault growth. The term *structural complexity* refers to the fracture abundance and range of orientations exhibited in a damage zone. We use the terms *simple* and *complex* as relative descriptions of the structural complexity of each damage zone, with complex indicating greater fracture abundances often displaying a wider range of orientations.

3. Geological setting

The Maltese Islands (Malta, Gozo, and Comino; Fig. 1a) are situated on the Malta Platform, which forms the NNE shoulder of the Late Miocene-Early Pliocene Pantelleria Rift (Reuther and Eisbacher, 1985; Dart et al., 1993; Jolivet and Faccenna, 2000). The archipelago is dominated by an ENE-WSW trending horst and graben system, comprising of the North Gozo and North Malta grabens (Dart et al., 1993; Putz-Perrier and Sanderson, 2010), that was activated during the Miocene before reaching a peak in activity during the Pliocene-Quaternary (Illies, 1981; Bosence and Pedley, 1982; Finetti, 1984; Jongsma et al., 1985). Major and minor extensional faults on the islands generally follow the trend of the horst and graben system with the exception of the ESE-WNW trending Il Maghlaq Fault (IMF; Fig. 1a), located on the southern coast of Malta, which has a similar trend to the Pantelleria Rift (Pedley et al., 1976; Illies, 1981; Reuther and Eisbacher, 1985; Bonson et al., 2007; Rotevatn et al., 2016). The Victoria Lines Fault (VLF) is a large graben-bounding fault (up to 195 m displacement) that separates the North Malta Graben from the Malta Horst to the south (Fig. 1a). The small extensional faults (<10 m displacement) that form the basis of this study are located at Ras ir Raheb, about 500–1000 m into the footwall of the VLF on the Malta Horst (Dart et al., 1993; Putz-Perrier and Sanderson, 2010; Michie et al., 2014; Dimmen et al., 2017). These small extensional faults may be considered as part of a >2 km wide footwall damage zone associated with the VLF, which includes several large splay faults distributing the displacement of the VLF (Putz-Perrier and Sanderson, 2010, Fig. 1a).

The islands comprise a sequence of Oligocene and Miocene carbonates that have a well-defined stratigraphy (Pedley et al., 1976; Dart et al., 1993). Along the coast at Ras ir Raheb (Fig. 1b), the stratigraphy can be divided into the Oligocene platform carbonates of the Lower Coralline Limestone Formation (LCLF) and the Miocene pelagic carbonates of the Globigerina Limestone Formation (Dart et al., 1993), which provide excellent outcrops for detailed studies of damage zones of small-scale extensional faults (e.g. Putz-Perrier and Sanderson, 2010; Dimmen et al., 2017). The Globigerina Limestone Formation can be divided into the Lower Globigerina Limestone Member (LGLM) and the Middle Globigerina Limestone Member (MGLM). The LGLM consists of fossiliferous packstones and wackestones and is marked at the top by a 50 cm thick phosphoritic conglomerate with an abundance of bivalve-, bryozoan-, solitary coral-, and echinoid-fossils (Pedley, 1987). The MGLM consists of highly bioturbated mudstones interbedded with thin layers (50–100 cm thick) of

phosphoritc conglomerate (Pedley et al., 1976; Bennett, 1979). The studied fault damage zones described in this study include relay- and tip-damage zones observed in plan-view on pavement outcrops of the MGLM and splay-damage zones observed in cross-section in cliff outcrops of both the LGLM and MGLM (Fig. 1b).

4. Methodology

4.1. Mapping of damage zones

Field outcrops of 6 tip-damage zones, 9 relay-damage zones and 3 splay-damage zones were identified and documented in detail along sub-horizontal pavements and cliffs of the Globigerina Limestone Formation at Ras ir Raheb (Nærland, 2016) (Fig. 1b). All fault damage zones were photographed, mapped and structurally characterised allowing them to be classified depending on their structural complexity. Structural data were collected for faults exposed along the coast, including fault plane orientations and measured fault displacements. The high-resolution outcrop images were then merged, imported and georeferenced in ArcGIS where the fracture networks associated with each fault damage zone were then digitised for further geospatial and topological analysis (e.g. Nyberg et al., 2018).

4.2. Network topology and assessing connectivity

A topological analysis was applied to each digitised fault damage zone in order to characterise the networks within them and to constrain their connectivity. In topology, each two-dimensional fracture network is considered as a planar graph consisting of nodes and branches between nodes (Manzocchi, 2002; Sanderson and Nixon, 2015; Sanderson et al., 2019). Based on the relationships between the fractures we can identify 3 types of node: *I*-nodes representing the tip of a fracture; *Y*-nodes representing the point of splaying or abutting fractures; and *X*-nodes representing the intersection point between two crossing fractures. Therefore, *Y*- and *X*-nodes are connecting nodes whereas *I*-nodes are isolated (Fig. 3a). As branches have one node at each end they can be classified into three types, based on whether the nodes are connecting (*C*) or isolated (*I*): isolated branches (*II*), singly connected branches (*IC*) and doubly connected

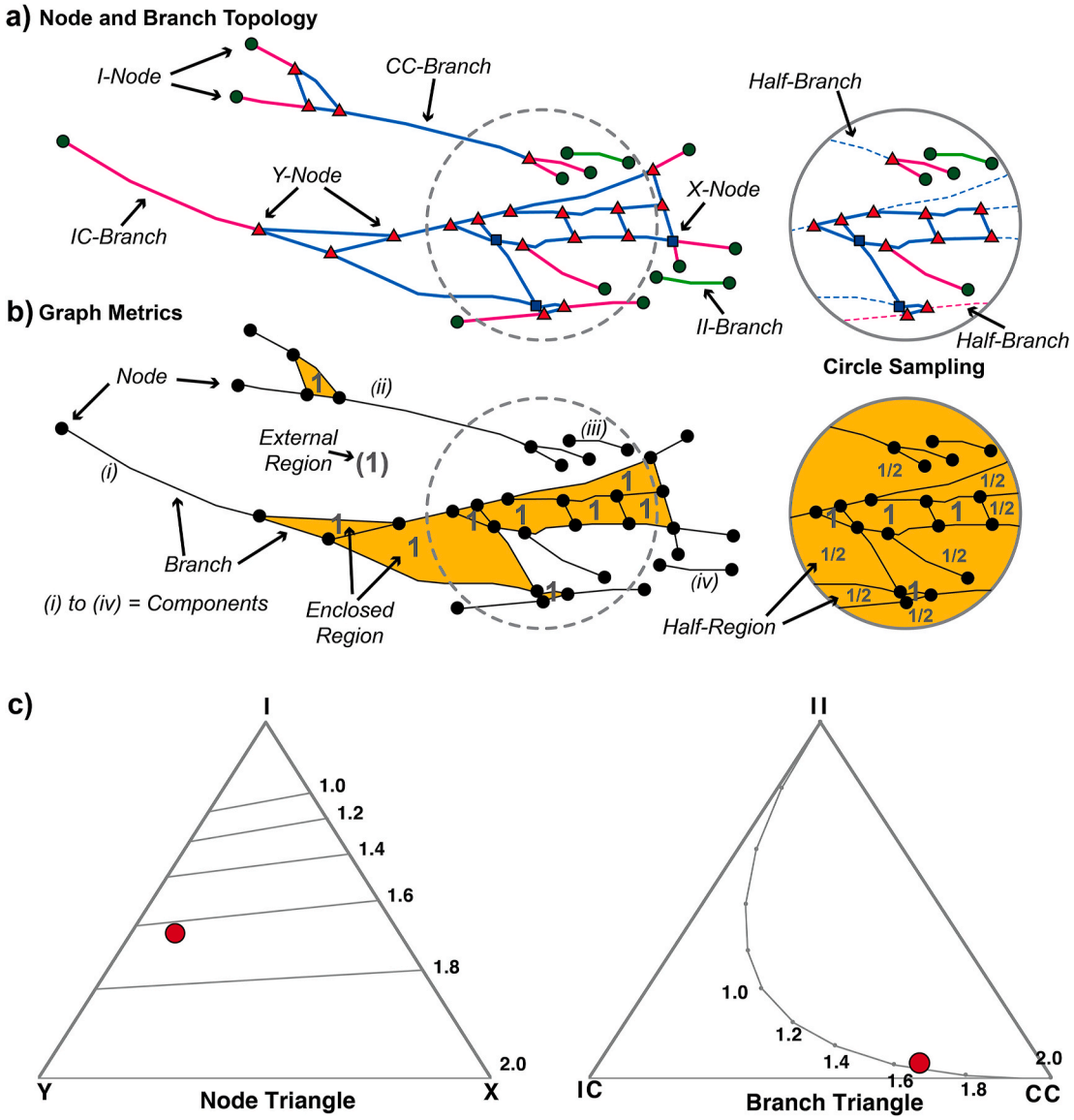

Fig. 3. a) Trace map of a fracture network illustrating different node and branch types. b) Graph representation of the same fracture network showing nodes (dots), branches (lines), regions (shaded) and components (i-iv). The circles to the right of the trace maps illustrate circle sampling of the different nodes, branches and regions. c) ternary diagrams of the different node and branch types with red dots representing the topology of the fracture network trace map in Fig. 3a. The contours represent the connections per branch and how this changes relative to the topology. (For interpretation of the references to colour in this figure legend, the reader is referred to the Web version of this article.)

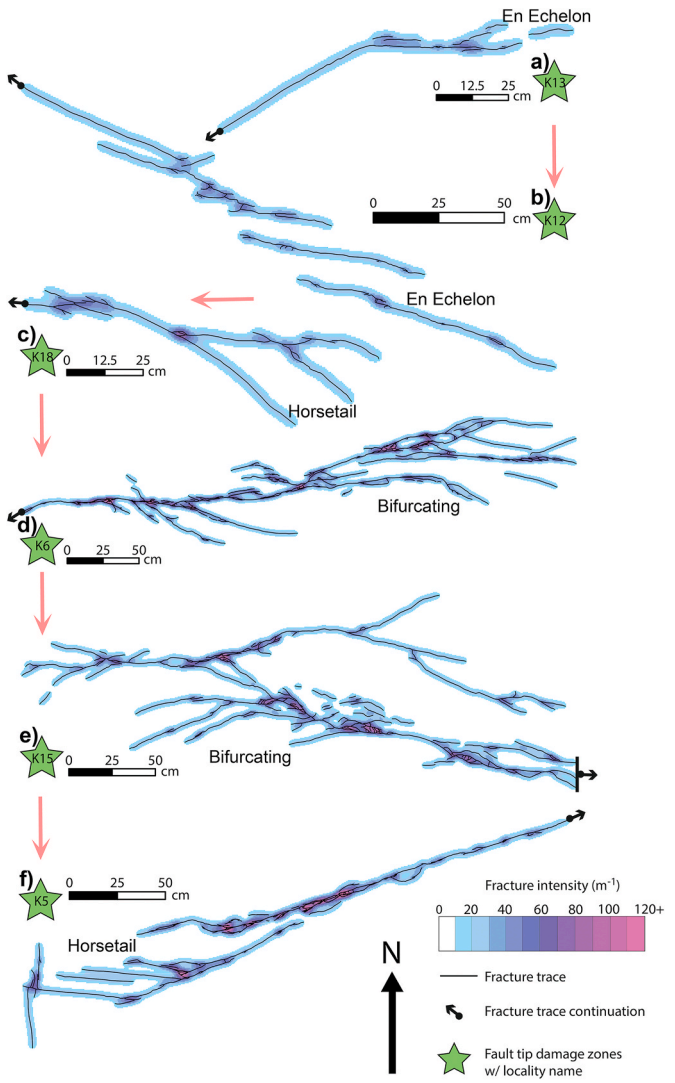

Fig. 4. Fracture trace maps of different fault tip-damage zones with their locality name and structural style labelled. The documented damage zones are all exposed in the MGLM. The damage zones are arranged according to the red arrows, which correspond to a relative increase in fracture intensity and connections per branch. These match the red arrows in the node and branch triangular plots in Fig. 7. (For interpretation of the references to colour in this figure legend, the reader is referred to the Web version of this article.)

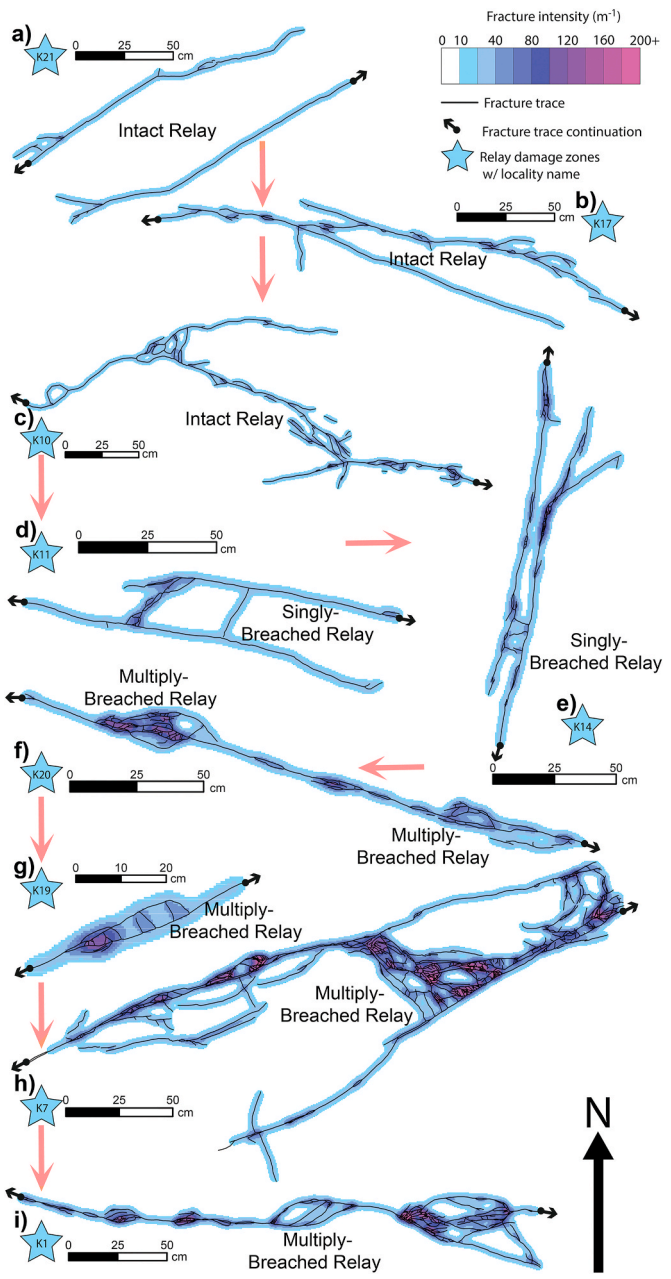

Fig. 5. Fracture trace maps of different fault relay-damage zones with their locality name and structural style labelled. The documented damage zones are all exposed in the MGLM. The damage zones are arranged according to the red arrows, which correspond to a relative increase in fracture intensity and connections per branch. These match the red arrows in the node and branch triangular plots in Fig. 7. (For interpretation of the references to colour in this figure legend, the reader is referred to the Web version of this article.)

branches (*CC*) (Sanderson and Nixon, 2015) (Fig. 3a). The number counts of each node type (N_I, N_Y, N_X) and branch type (B_{II}, B_{IC}, B_{CC}) can be used to plot their proportions on ternary diagrams, topologically characterising the fracture networks. The number of branches (B) and number of nodes (N) are related to each other by:

$$B = (N_I + 3N_Y + 4N_X) / 2 \quad (1)$$

It should be noted that when sampling topological elements, that branches extending beyond the sample area are counted as half-branches in this relationship as only one end node is visible.

Where a network plots in a ternary diagram is representative of the network's connectivity. Isolated and poorly connected networks will plot towards the *I*-node and *II*-branch corners of each ternary diagrams, whereas well connected networks will plot towards the *Y-X* axis and *CC* corner (Fig. 3). Furthermore, the number counts of the different node types can be used to calculate parameters that directly describe the degree of connectivity within a network such as *connections per branch* (C_B), which describes the degree of connectivity between branches:

$$C_B = (3N_Y + 4N_X) / B \quad (2)$$

As branches only have two nodes associated with them (i.e. *I* or *C*) values of C_B range from 0 to 2 and can also be contoured onto both the node and branch ternary diagrams (Fig. 3) (Sanderson and Nixon, 2015, 2018).

Another parameter is the *average degree* ($<D>$), which describes the degree to which nodes are connected to branches (Sanderson et al., 2019). It is defined by the ratio between the number of branches (B) and the number of nodes (N), whereby:

$$B / N = <D> / 2 \quad (3)$$

Thus $<D>$ provides an important link between the nodes and

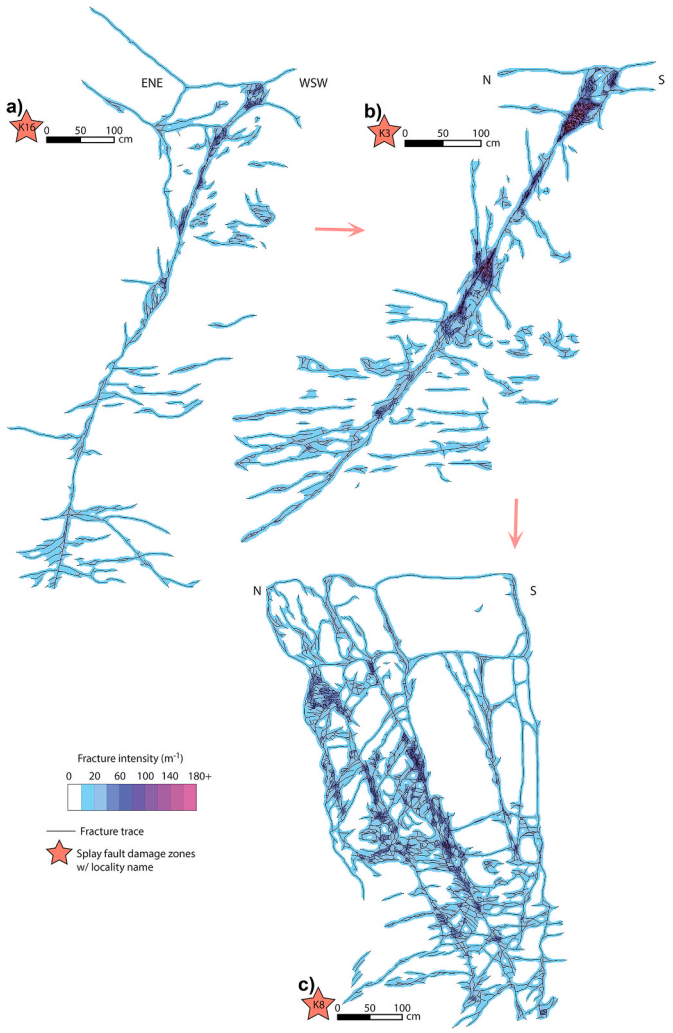

Fig. 6. Fracture trace maps of different fault splay-damage zones with their locality name and structural style labelled. These splay fault damage zones are all exposed in vertical outcrops of the LGLM and MGLM. The damage zones are arranged according to the red arrows, which correspond to a relative increase in fracture intensity and connections per branch. These match the red arrows in the node and branch triangular plots in Fig. 7. (For interpretation of the references to colour in this figure legend, the reader is referred to the Web version of this article.)

branches of the network. Within a fracture network an *I*-node has a degree of 1, a *Y*-node has a degree of 3 and an *X*-node has a degree of 4. Thus the average degree will vary from $<D> = 1$ (for poorly connected networks dominated by *I*-nodes and isolated branches) to $<D> = 4$ (for a completely connected network dominated by crossing fractures forming only *X*-nodes and *CC*-branches) (Fig. 3). Many natural fracture networks, particularly joint systems and fault networks, are often dominated by abutting relationships and Y-nodes (e.g. Nixon et al., 2012; Morley and Nixon, 2016; Duffy et al., 2017) and expected values of $<D>$ will likely lie between 1 and 3.

4.3. Euler's theorem, regions and components

In graph theory the arrangement of the different nodes and branches within each fracture network forms a planar graph (Sanderson et al., 2019). As well as nodes and branches each planar graph contains components and regions bounded by cycles (Fig. 3b). The simplest component is an isolated branch (i.e. components *iii* and *iv* in Fig. 3b) but numerous connected nodes and branches will produce a connected component (i.e. components *i* and *ii* in Fig. 3b). Connected components represent clusters of fractures and can form anything from finite tree-like clusters to infinite networks. Regions, on the other hand, are the enclosed spaces within connected components representing the blocks of rock between fractures (Sanderson et al., 2019).

Equation *(3)* shows that the number of branches (*B*) and number of nodes (*N*) can be linked to one another through the average degree ($<D>$). However, they can also be related to the number of components (*K*) and number of regions (*R*) through a generalisation of Euler's theorem (Euler, 1758; Sanderson et al., 2019), where by:

$$R = B - N + K \tag{4}$$

This indicates specific relationships between the different metrics (*R, B, N* and *K*) for a given network. In this paper we focus on comparing these different graph metrics to identify any relationships that could be useful for further classifying or describing the damage zones.

In addition, equation *(4)* is useful for extracting further metrics about a network. In particular, it can be used to extract the number of regions (or blocks between fractures) within each fracture network, simply calculated from the number of nodes, branches and connected components. If the area (*A*) of the extent of the sampled fracture network is known then we can also calculate an average block area (*A/R*) for the network (Sanderson et al., 2019). Furthermore, dividing the average block area by the total sample area will give the dimensionless block intensity (R_{22}), which can be simplified to:

$$R_{22} = A^{-1}.\ (A\ /\ R) = 1\ /\ R \tag{5a}$$

As *R* represents the number of enclosed regions, we can modify Equation *(5a)* to include an external infinite region representing the surrounding rock mass:

$$R_{22} = 1\ /\ (R + 1) \tag{5b}$$

Thus, from equation *(5b)*, values for R_{22} will range from 0 to 1, with 1 representing an intact rock mass that becomes more broken up as R_{22} tends to 0. Therefore, as well as characterising the topology and connectivity of each damage zone we can also constrain how broken up the rock mass is within each damage zone, hence, quantifying the amount of damage. It is worth noting that this measure is highly influenced by the observed extent of a network and thus should only be used when comparing entire networks or sample areas of the same size.

4.4. Sampling and assessing spatial variability

As well as collecting geometric and topological data for the damage zone as a whole, we also subsampled each damage zone to assess spatial variability. Circle samples that eliminate orientation bias (Mauldon et al., 2001; Sanderson and Nixon, 2015) were used to subsample along-strike and dip of the main faults associated with each damage zone. Within each circle sample the area, total trace-length, and the number of different topological elements (nodes, branches, components and regions) were recorded.

The sampling of nodes is straight forward as you simply count the number of nodes that lie within each circle sample (Fig. 3a). However, a branch may go beyond the boundary of a sample area, which means that: a) the length of such a branch is unknown or censored; and b) only one node associated with the branch lies within the sample area. Such branches can only be counted as half-branches. If topological information for the surrounding network is known, then the topology of the half-branch can still be determined. However, if this information is unknown then the topology of the branch cannot be determined and is classified as unknown. If a branch passes through a circle sample area then its associated nodes do not lie within the sample, thus the branch is not included in the branch count. This approach ensures that the branch count is consistent with the number of branches (*B*) calculated from the node count in equation *1*. When calculating the number of regions (*R*) for each circle sample, using equation *4,* we assume that the network is part of one connected component (after excluding isolated branches) as the components may be connected outside the sample area. Thus $R = B - N + 1$, resulting in a minimum value for the

number of regions within each circle. Furthermore, a consequence of counting half-branches is that the value of R will include complete regions, within the circle sample, as well as half-regions which leave the sample area (Sanderson et al., 2019).

The recorded circle sample data were used to calculate subsequent along-strike/along-dip profiles of different parameters including: i) fracture intensity, defined as total fracture trace-length per unit area (m^{-1} or m/m^2); ii) connecting node frequency, defined as the number of connections per unit area (N_C/m^2); and iii) the dimensionless block intensity (R_{22}). In addition, contour plots of fracture intensity and connecting node frequency are used to illustrate variations within each damage zone.

5. Results

5.1. Structural description of the damage zones

All of the studied damage zones are associated with normal faults, with

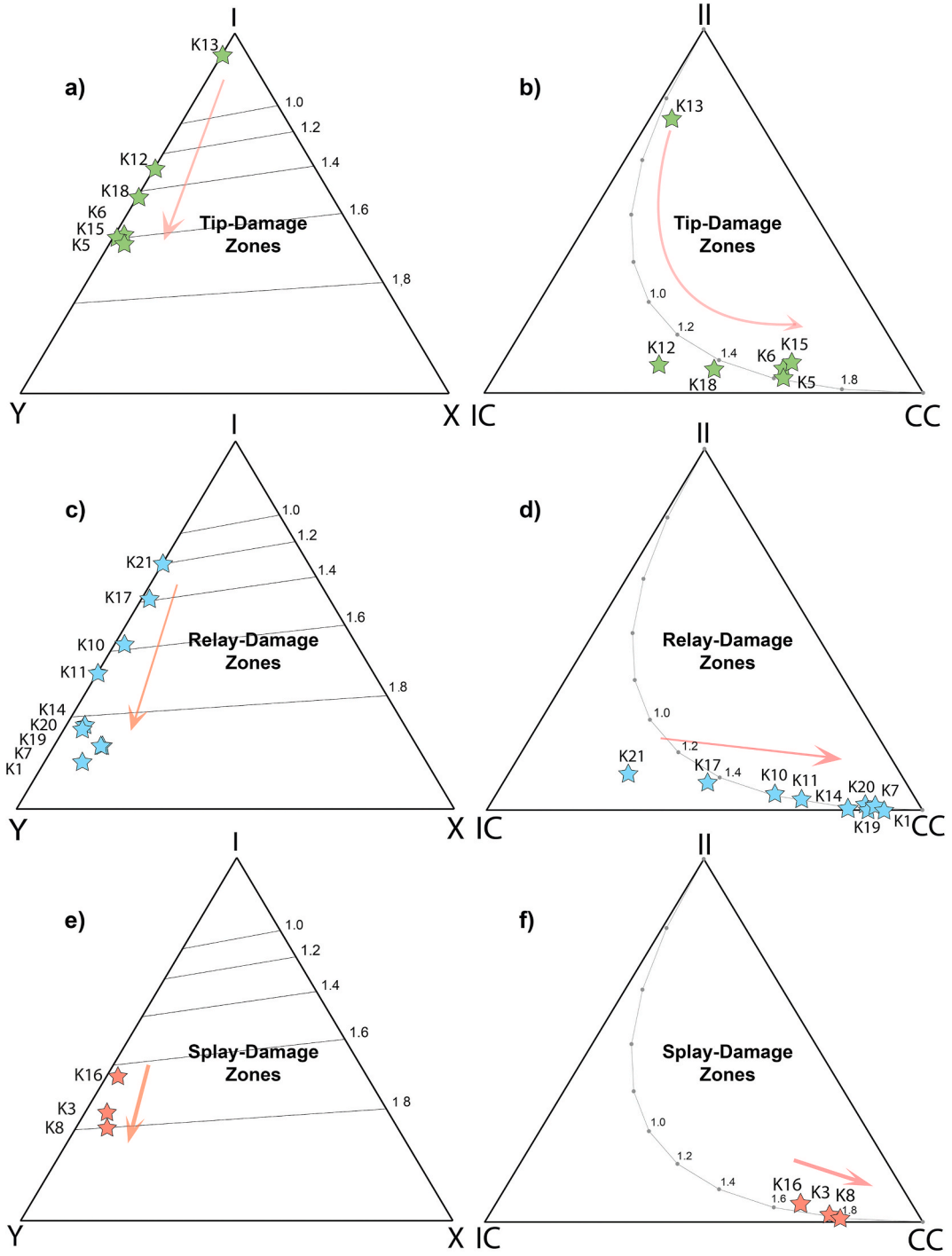

Fig. 7. Node and branch triangular plots of each damage zone example. Fault tip-damage zones are presented in a) and b); Relay-damage zones are presented in c) and d); and splay-damage zones are presented in e) and f). The node triangles (left) illustrate the proportions of *I*-, *Y*- and *X*-nodes mapped for each damage zone. The branch triangles (right) illustrate the proportions of *II*-, *IC*-, and *CC*-branches mapped for each damage zone. The locality name of each damage zone is indicated and the red arrows correspond with the arrangement of the fracture trace maps in Figs. 4–6. (For interpretation of the references to colour in this figure legend, the reader is referred to the Web version of this article.)

Table 1
Topology and graph data for each fault damage zone example including: node and branch type proportions; graph metrics, i.e. number of nodes (*N*), branches (*B*), components (*K*) and regions (*R*); average degree (<*D*>); connections per branch (C_B). See text for definitions and derivation.

Field Example	Damage Zone Type	Node Proportions			Branch Proportions			Graph Metrics				Degree of Connectivity	
		I	Y	X	II	IC	CC	N	B	K	R	<D>	C_B
K12	Tip - En Echelon	63%	37%	0%	8%	56%	36%	51.5	47.5	4	0	1.8	1.3
K13	Tip - En Echelon	89%	11%	0%	70%	9%	22%	3.5	3.5	1	1	2.0	0.5
K5	Tip - Horsetail	42%	55%	3%	4%	30%	66%	218	251	4	37	2.3	1.6
K6	Tip - Bifurcating	44%	55%	2%	6%	28%	65%	306	356	6	56	2.3	1.6
K15	Tip - Bifurcating	45%	53%	2%	8%	26%	66%	209.5	244.5	3	38	2.3	1.6
K18	Tip - Horsetail	55%	45%	0%	6%	44%	49%	29.5	29.5	2	2	2,0	1.4
K10	Relay - Intact	44%	55%	1%	5%	31%	64%	108	121	3	16	2.2	1.6
K17	Relay - Intact	57%	41%	2%	8%	46%	47%	48.5	48.5	4	4	2.0	1.4
K21	Relay - Intact	67%	33%	0%	10%	60%	30%	21	18	3	0	1.7	1.2
K11	Relay - Singly Breached	38%	63%	0%	3%	26%	71%	32	35	1	4	2.2	1.7
K14	Relay - Singly Breached	23%	73%	4%	1%	17%	83%	106.5	136.5	2	32	2.6	1.8
K20	Relay - Multiply Breached	22%	74%	4%	2%	12%	86%	151.5	202.5	2	53	2.7	1.8
K1	Relay - Multiply Breached	13%	79%	9%	0%	9%	91%	294.5	413.5	2	121	2.8	1.9
K7	Relay - Multiply Breached	17%	72%	11%	1%	10%	89%	888	1242.5	3	357.5	2.8	1.9
K19	Relay - Multiply Breached	17%	72%	10%	0%	13%	88%	30	40	1	11	2.7	1.9
K3	Splay	30%	65%	5%	2%	20%	78%	2665	3352	33	720	2.5	1.8
K8	Splay	26%	67%	7%	1%	18%	81%	2851.5	3696.5	11	856	2.6	1.8
K16	Splay	40%	58%	2%	5%	25%	70%	715	848.5	22	155.5	2.4	1.6

less than 1.5 m of displacement, and consist of smaller faults (displacements up to a few cm) and opening-mode fractures. The faults generally have steep dips (up to 85°) and form a bimodal fault population with conjugate sets trending NNE-WSW and ESE-WNW (Fig. 1b). The examples of each type of fault damage zone (tip-, relay-, splay-) show varying degrees of structural complexity and can be further classified based on their structural style (Figs. 4–6).

We identify three different tip-damage zones with the simplest en echelon tips comprising overlapping and stepping fractures (e.g. Fig. 4a and b). More structurally complex tips include horsetail tips (e.g. Fig. 4c and f) that form several obliquely splaying fractures along-strike of the fault tip, and bifurcating tips (e.g. Fig. 4d and e) that include numerous splaying and intersecting fault strands and fractures. Local fracture intensities range spatially from 10 m^{-1} to 120 m^{-1} with the more complex tip damage zones exhibiting the highest intensities, often located at splays or areas of intense bifurcation, whereas the simplest tip damage zones only exhibit intensities <80 m^{-1} (e.g. Fig. 4a–c).

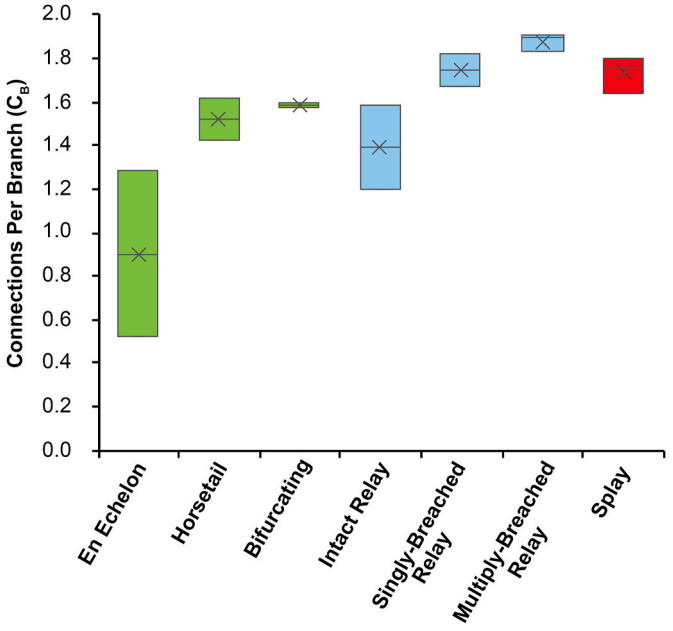

Fig. 8. Box plots illustrating the range (box), mean (cross) and median (line) in connections per branch for each type and style of damage zone. Green, blue and red boxes correspond to tip-, relay- and splay-damage zones respectively with different structural styles are listed along the x-axis. (For interpretation of the references to colour in this figure legend, the reader is referred to the Web version of this article.)

The relay-damage zones are divided into intact relays, singly-breached relays and multiply-breached relays (Fig. 5). Intact relays comprise overlapping fault segments that may be interacting but have no physical linkage between the segments across the entire relay ramp. In the singly-breached relays, the fault segments are overlapping and interacting with a single linking fault/fracture crossing the relay ramp between the two segments. Multiply-breached relays are where the two fault segments are linked by two or more faults/fractures, thus breaking up the relay ramp creating a more complex damage zone. Local fracture intensities range spatially from 10 m^{-1} to 200 m^{-1} with the intact relay damage zones exhibiting the lowest intensities of <80 m^{-1} and the singly-breached relays containing intensities up to 100 m^{-1} (Fig. 5d and e). The highest intensity values are exhibited by the more complex multiply-breached relays (Fig. 5f–i), with greatest intensities restricted to linkage areas where faults/fractures are either splaying from or abutting the main fault segments.

Splay-damage zones can range in complexity from a main fault with one or two synthetic splay faults (Fig. 6a and b) to a main fault with several synthetic splay faults interconnected by numerous antithetic faults/fractures (Fig. 6c). The examples in this study show local fracture intensities ranging from 10 to 180 m^{-1}, with K16 being the least structurally complex and exhibiting the lowest fracture intensities. In general local fracture intensities are less than 100 m^{-1}, however, much higher values are observed at lenses and around splay intersections as shown for examples K3 and K8 (Fig. 6).

5.2. Damage zone topology and connectivity

In the next sections, we will explore the topology and graph metrics of the three main types of fault damage zone (tip-, relay- and splay-). The triangular plots in Fig. 7, along with Table 1, illustrate the proportions of the different node and branch types of each studied damage zone. The damage zones are mostly dominated by *I*- or *Y*-nodes, but show a broad variation plotting close to the *I–Y* axis. Furthermore, almost all the damage zones are dominated by *IC*- or *CC*-branches, so plotting close to the *IC-CC* axis of the branch triangle.

The fault tip-damage zones (Fig. 4) plot closer to the *I*-node corner of the node triangle than relay- and splay-damage zones (Fig. 7a). Example K13, an en echelon tip, exhibits the greatest proportion of *I*-nodes at ~95%

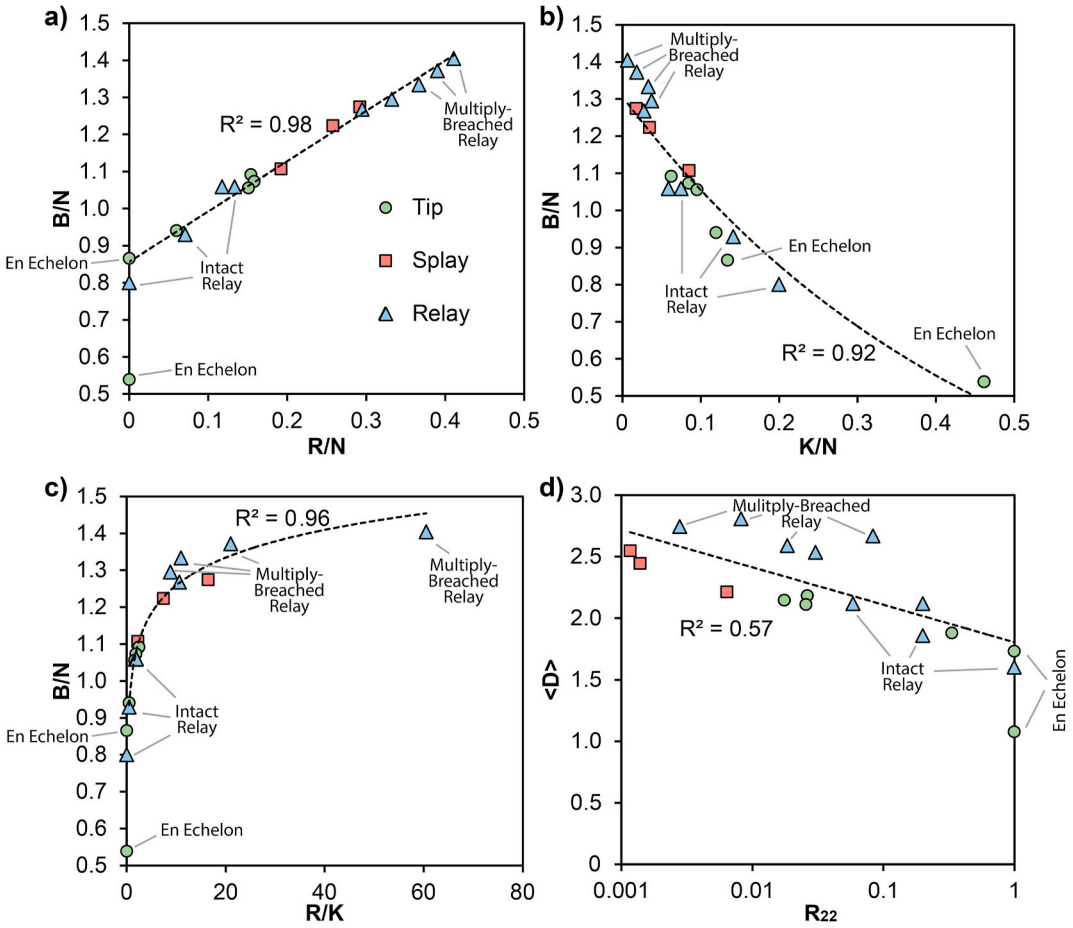

Fig. 9. Scatter plots comparing different graph metrics for each tip-damage zone (green circles), relay-damage zone (blue triangles) and splay-damage zone (red squares). a) Plot of the ratio of branches to nodes (*B/N*) against the ratio of regions to nodes (*R/N*); b) Plot of the ratio of branches to nodes (*B/N*) against the ratio of components to nodes (*K/N*); c) Plot of the ratio of branches to nodes (*B/N*) against the ratio of regions to components (*R/K*); d) Plot of the average degree (<*D*>) against the dimensionless block intensity (R_{22}). Note that values for *B/N* correspond to <*D*>/2. (For interpretation of the references to colour in this figure legend, the reader is referred to the Web version of this article.)

and is one of three tip-damage zones with no *X*-nodes (i.e. K13, K12, K18; Fig. 7a and Table 1). Whereas example K5, a horsetail tip, has the highest proportion of *Y*-nodes (~55%) and *X*-nodes (~3%) of all six fault tip-damage zones (Fig. 7a and Table 1). The branch triangle shows that most of the fault tip-damage zones plot along the *IC-CC* axis with low proportions of *II*-branches, between 4% and 8% (Fig. 7b and Table 1). The en echelon tip, K13, is the only fault damage zone dominated by *II*-branches with a proportion of >70%, thus plotting in the *II*-branch corner of the triangle. The en echelon tips produce the most isolated branches and nodes due to their unlinked and stepping fracture arrays. The nature of the bifurcating and horsetail tips, with numerous splaying and branching fractures, mean they have greater potential for creating *Y*-nodes and *IC*- or *CC*-branches.

The relay-damage zones (Fig. 5) plot closer to the *Y*-node corner of the triangle than both tip- and splay-damage zones (Fig. 7c). However, the examples show a large spread in node topology with examples K17 and K21, both intact relays, dominated by *I*-nodes with proportions of 57% and 67%, respectively. In contrast, the singly- (K11, K14) and multiply-breached relays (K1, K7, K19, K20) are all dominated by *Y*-nodes, with the latter showing the greatest proportion of connecting nodes (>80% *Y*- and *X*-nodes; Fig. 7c and Table 1) than any of the studied damage zones. Note that the multiply-breached relays also have greater proportions of *X*-nodes (between 8% and 11%) than any other damage zones. The relay-damage zones are dominated by *IC*- and *CC*-branches, with proportions of *II*-branches at <10%. The intact relays (K10, K17, K21; Fig. 7d and Table 1) exhibit more *IC*-branches (>30%) than the other relay-damage zones, with multiply-breached relays exhibiting up to 91% *CC*-branches, which is much greater than the other types of damage zone. The results indicate a progressive increase in both the proportion of connecting nodes (*Y*- and *X*-nodes) and *CC*-branches from intact relays to singly-breached relays to multiply-breached relays. These differences are a result of differences in their structural style with intact relays displaying more bifurcating fractures producing more *IC*-branches. Whereas the singly- and multiply-breached relays produce linking fractures between the two fault segments thus creating more *CC*-branches and less *I*-nodes.

Splay-damage zones are clustered in both the node and the branch plots, reflecting a low variability in topology (Fig. 7e and f). They generally have topologies more similar to the relay-damage zones than the tip-damage zones (Fig. 7). The node plot shows that the splay-damage zones have large proportions of connecting nodes, ranging from ~60% to ~74% (Table 1). There are also very few *II*-branches (<6%) within the splay-damage zones with the largest proportion of their branches being fully connected *CC*-branches (>70%; Fig. 7f and Table 1).

The differences in topology between the three types of fault damage zone are reflected in the number of connections per branch (C_B; Fig. 8 and Table 1), with tip-damage zones having the lowest range of C_B (0.52–1.62), with en echelon tips forming the least connected fracture networks ($C_B < 1.30$; Fig. 8). Horsetail and bifurcating tips produce better connected tip-damage zones with values of $C_B > 1.40$. In the relay-damage zones C_B increases from less connected intact relays to very connected multiply-breached relays (Fig. 8). Intact relays display a similar range of C_B to the tip-damage zones as they comprise two overlapping but soft linked

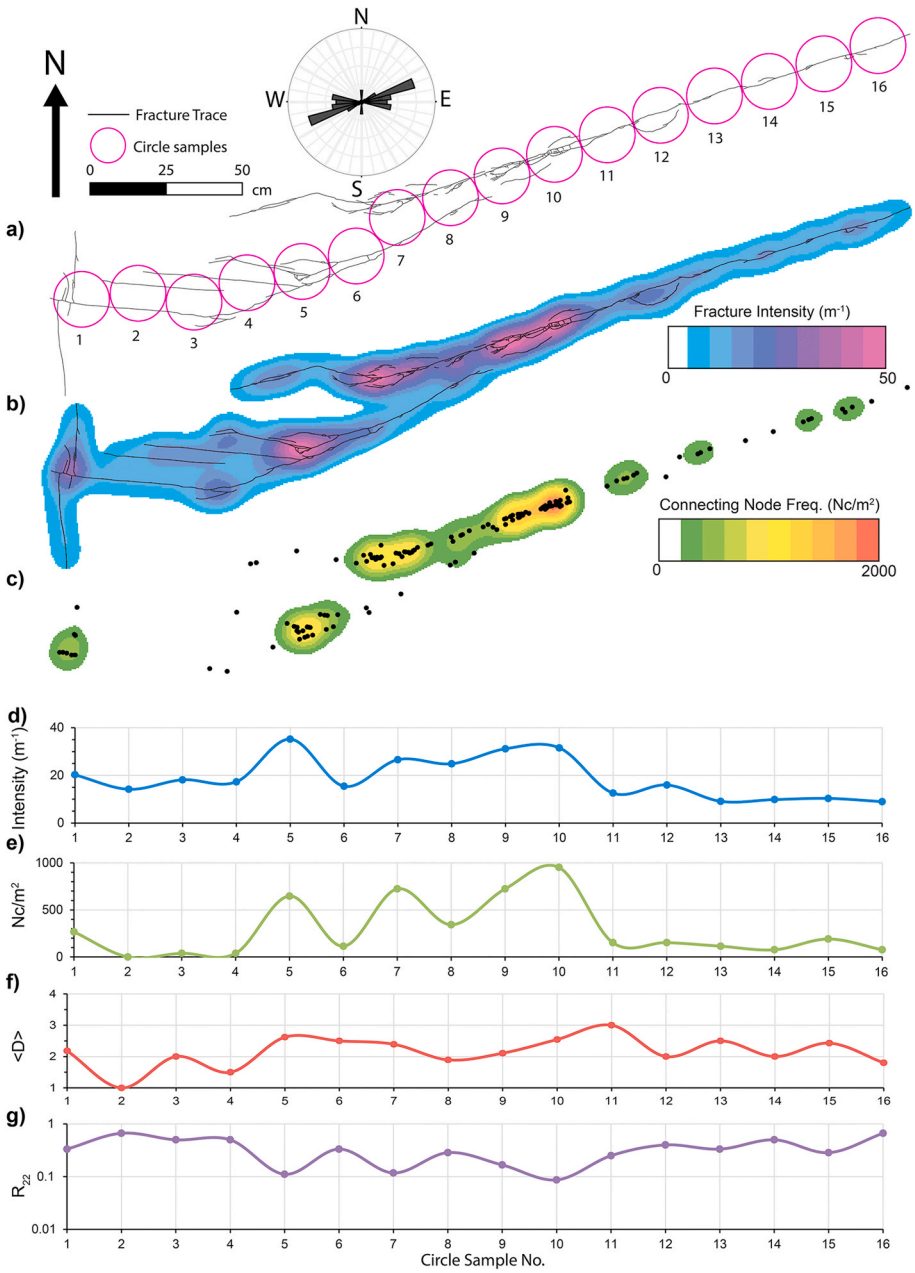

Fig. 10. a) Digitised fracture trace map of the tip-damage zone at locality K5 showing the position of 16 circle samples and a length-weighted rose diagram of the fracture trends. b) Contour map, showing the fracture abundance measure "fracture intensity". c) Contour map showing the topological parameter "connecting node frequency". d) Along strike profile of fracture intensity measured in each circle sample in Fig. 10a e) Along strike profile of connecting node frequency (Nc/cm^2) measured in each circle sample in Fig. 10a f) Along strike profile of average degree ($<D>$) measured in each circle sample in Fig. 10a g) Along strike profile of the dimensionless bock intensity (R_{22}) measured in each circle sample in Fig. 10a.

fault tips. In contrast, multiply-breached relays are the most connected damage zone examples with values of $C_B > 1.85$, which can be expected from hard linked fault segments. Splay-damage zones also produce well connected fracture networks with values of $C_B > 1.60$, similar to singly-breached relays (Fig. 8).

5.3. Graph metrics

The plots in Fig. 9 compare various graph metrics (i.e. number of nodes, branches, regions and compartments; Table 1) of the different damage zone fracture networks. Fig. 9a and b compare the number of branches (B) to the number of regions (R) and components (K), respectively. These metrics are normalised to the total number of nodes (N), which accounts for different sizes of network (i.e. larger networks produce greater numbers of nodes). Furthermore, this produces the parameter B/N (number of branches per node or branch to node ratio) on the y-axis, which is the equivalent of $<D>/2$, thus linking to the degree of connectivity. The plots indicate clear relationships where an increase in the branch to node ratio (B/N) results in an increase in the number of regions (Fig. 9a) and a decrease in the number of components (Fig. 9b). The combined effect of these relationships means that the number of regions per component (R/K) within each damage zone increases with the ratio of branches to nodes (B/N) (Fig. 9c). This increase in the regions per component does not begin until the fracture networks reach a branch to node ratio of 0.9 (Fig. 9c), equivalent to an average degree ($<D>$) of 1.8, as no regions form below this degree of connectivity (Fig. 9a).

The tip-damage zones form fracture networks with low numbers of regions (Fig. 9a) but have high numbers of components (Fig. 9b). This is particularly the case for en echelon tips which form no regions (Fig. 9a) but have large proportions of isolated (I) and singly connected (IC) branches (e.g. Figs. 4 and 7b). As a result, they produce the lowest branch to node ratios ($B/N < 0.9$). The relay-damage zones show a large spread in graph metrics with intact relays overlapping with tip-damage zones, so producing less regions but more components in comparison to the singly-breached and multiply-breached relays (Fig. 9a and b). The multiply-breached relays produce the most number of regions and least number of components of all the studied damage zones, resulting in the highest

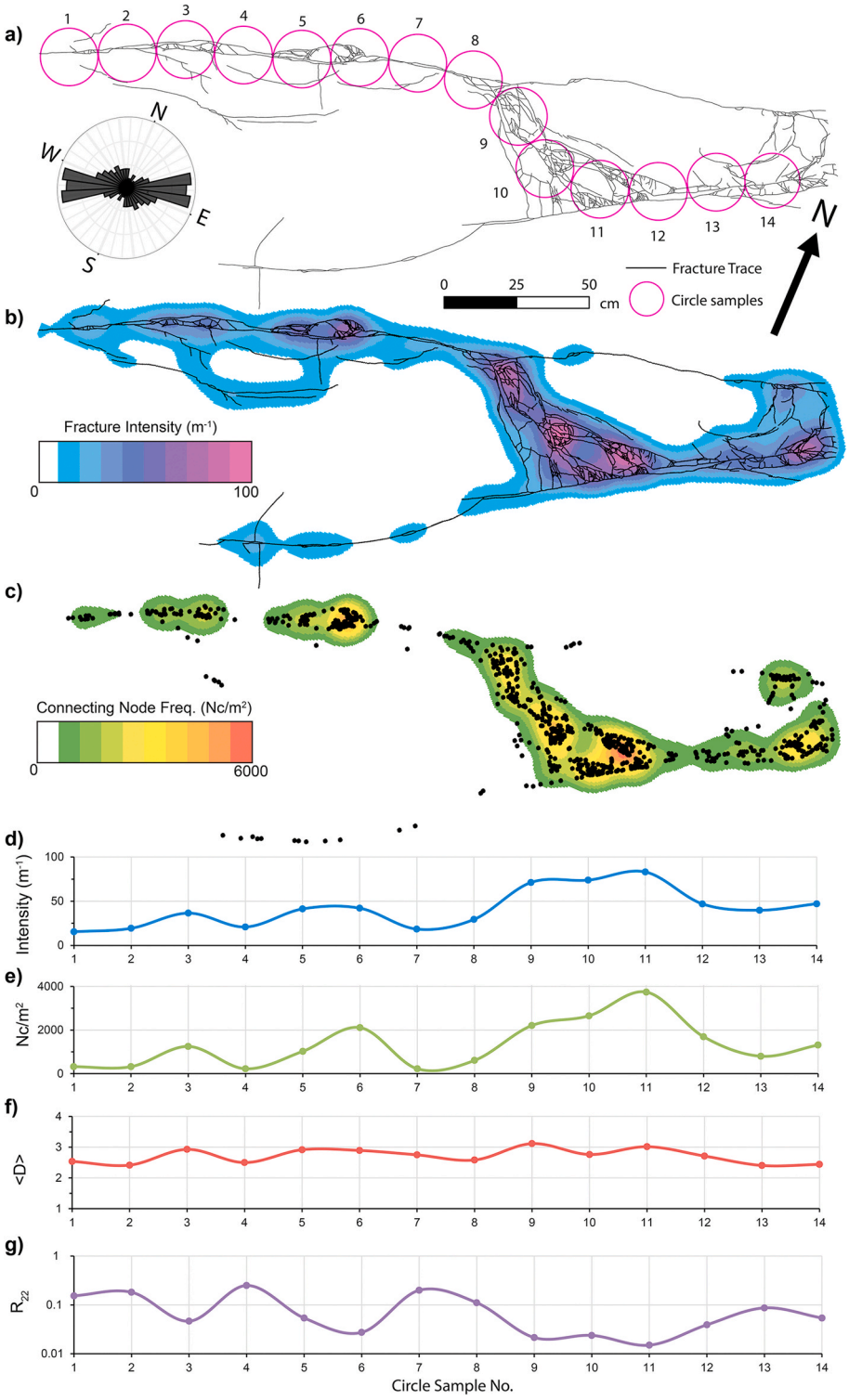

Fig. 11. a) Digitised fracture trace map of the relay-damage zone at locality K7, showing the position of 14 circle samples and a length-weighted rose diagram of the fracture trends. b) Contour map, showing the fracture abundance measure "fracture intensity". c) Contour map showing the topological parameter "connecting node frequency". d) Along strike profile of fracture intensity measured in each circle sample in Fig. 11a e) Along strike profile of connecting node frequency (Nc/cm^2) measured in each circle sample in Fig. 11a f) Along strike profile of average degree ($<D>$) measured in each circle sample in Fig. 11a g) Along strike profile of the dimensionless bock intensity (R_{22}) measured in each circle sample in Fig. 11a.

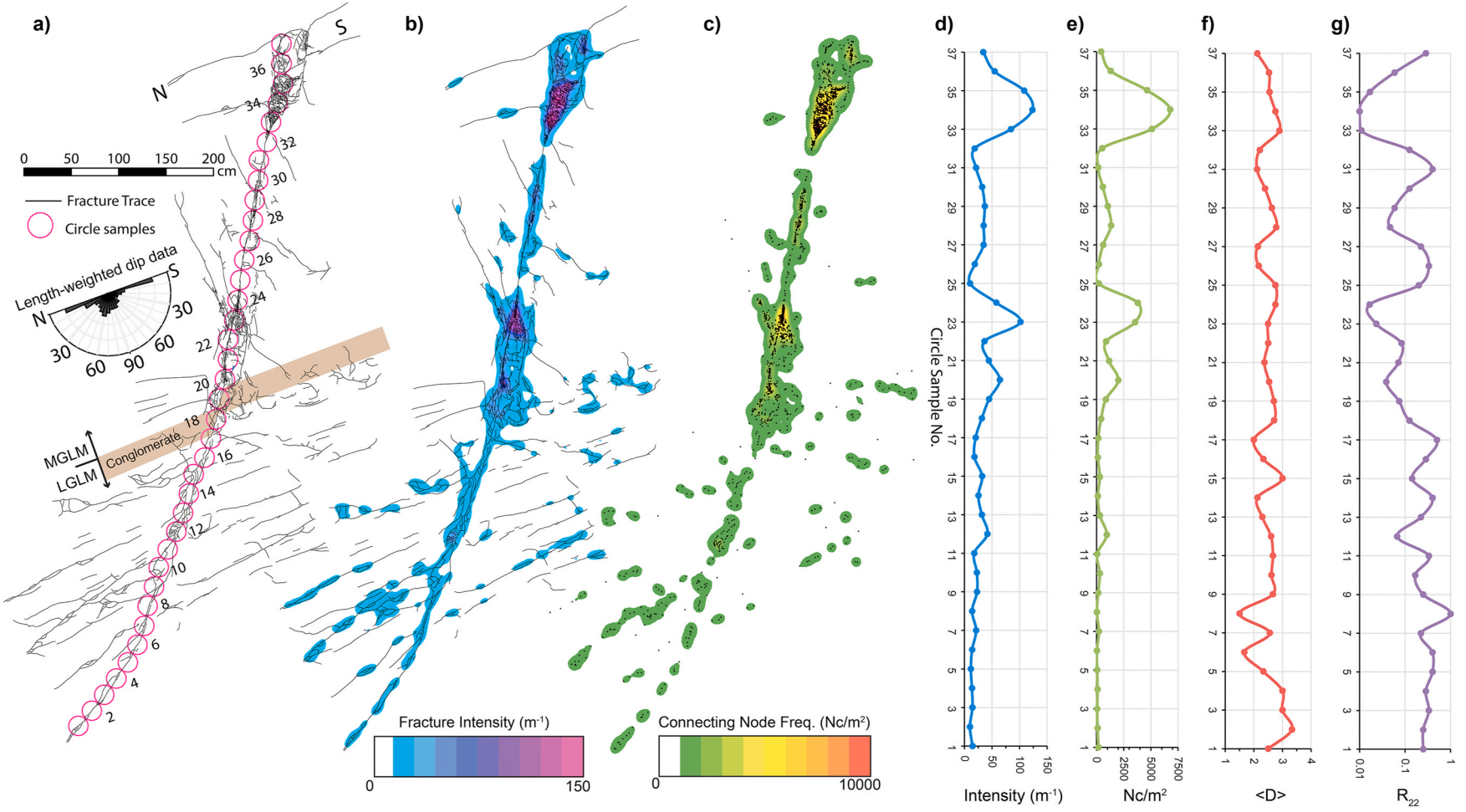

Fig. 12. a) Digitised fracture trace map of the splay-damage zone at locality K3, showing the position of 37 circle samples and a length-weighted rose diagram of the fracture dip trends. Note that the boundary between the MGLM and LGLM is indicated as well as the position of a phosphoritic conglomerate. b) Contour map, showing the fracture abundance measure "fracture intensity". c) Contour map showing the topological parameter "connecting node frequency". d) Along-dip profile of fracture intensity measured in each circle sample in Fig. 12a e) Along-dip profile of connecting node frequency (Nc/cm^2) measured in each circle sample in Fig. 12a f) Along-dip profile of average degree ($<D>$) measured in each circle sample in Fig. 12a g) Along-dip profile of the dimensionless bock intensity (R_{22}) measured in each circle sample in Fig. 12a.

number of regions per component (Fig. 9c). Splay-damage zones show the least spread in graph metrics with relatively moderate numbers of regions and low numbers of components (Fig. 9a and b), thus displaying similar characteristics to the singly- and multiply-breached relays.

Overall there appears to be a trend where, relative to the size of their networks, the more structurally complex damage zones (i.e. singly- and multiply-breached relays) produce more regions per component than for simple damage zones (i.e. en echelon tips and intact relays). This relationship is reflected in Fig. 9d, which illustrates influence of the degree of connectivity, with the dimensionless block intensity (R_{22}) tending to 1 as the average degree ($<D>$) decreases towards 1.8. This suggests simple en echelon tips leave the rock mass relatively intact ($R_{22} = 1$), as they produce no blocks, whereas the more complex multiply-breached relays break it into many blocks ($R_{22} \ll 1$). The fracture networks of splay-damage zones show the lowest values of R_{22} (<0.01), suggesting they produce the most amount of damage in comparison to the other damage zones.

5.4. Spatial variations in topology and damage

One example of each type of damage zone (tip-, relay-, splay-) is selected for full presentation to explore the spatial distribution of different topological parameters and fracture abundances. Specifically, we use contour maps in combination with circle samples (CS) that record along-strike/along-dip profiles in fracture intensity, connecting node frequency, average degree ($<D>$) and the dimensionless block intensity (R_{22}) (Figs. 10–12). We focus on describing the locations of structurally complex areas, with high fracture intensities and a range of fracture orientations, within each type of damage zone and their relationship with topological and graph measures.

5.4.1. Fault tip damage zone: example K5

Example K5 is a small (max. throw: 1 cm) NNW-dipping normal fault exposed in a pavement outcrop within the MGLM (Fig. 1b). The normal fault tip comprises two main fault segments, that are soft linked, and splays into a set of WNW-trending wing-cracks (Fig. 10a). The fracture intensity map (Fig. 10b) shows values mostly below 20 m^{-1}, with bullseyes of higher values restricted to bifurcation points (e.g. CS5, CS7 and CS8; Fig. 10a) or areas of lensing (e.g. CS9 to CS10; Fig. 10a) within the main part of the tip-damage zone. Bullseyes in the connecting node frequency map are also restricted to areas of bifurcation and lensing (Fig. 10c). This relationship is reflected on along-strike profiles of fracture intensity (Fig. 10d) and connecting node frequency (Fig. 10e) with corresponding peaks at CS5, CS7 and CS10.

Values of R_{22} are >0.1, indicating a low to moderate amount of damage, but show a clear inverse relationship to connecting node frequency and fracture intensity with lows at CS5, CS7 and CS10. This indicates that these areas of bifurcation and lensing within the damage zone are sites of increased damage where high fracture abundances and numbers of connections break the rock mass into numerous blocks. Values for $<D>$ vary from 1 to 3, forming a broadly undulating but consistent profile with a decrease towards end of the tip zone from CS4 to CS1. They do not appear to correlate directly with the other profiled measures suggesting that the degree of connectivity is spatially less variable and not directly related to local increases in fracture intensity and connecting node frequency.

5.4.2. Relay damage zone: example K7

Example K7 is a small (max. throw: 8 cm) multiply-breached relay, exposed in a pavement outcrop within the MGLM (Fig. 1b), between two right-stepping ENE-trending normal faults that dip towards NNW. Within the relay-damage zone, a wide range of fracture orientations are observed with ~NW-trending faults/fractures breaching across the relay (Fig. 11a). Fracture intensities are generally less than 50 m^{-1} along the relay bounding faults with minor bullseyes and peaks associated with lensing (i.e. CS3, CS5 and CS6; Fig. 11b and d). The highest intensity values (>50 m^{-1}) are observed along the relay breach with bullseyes where breaching

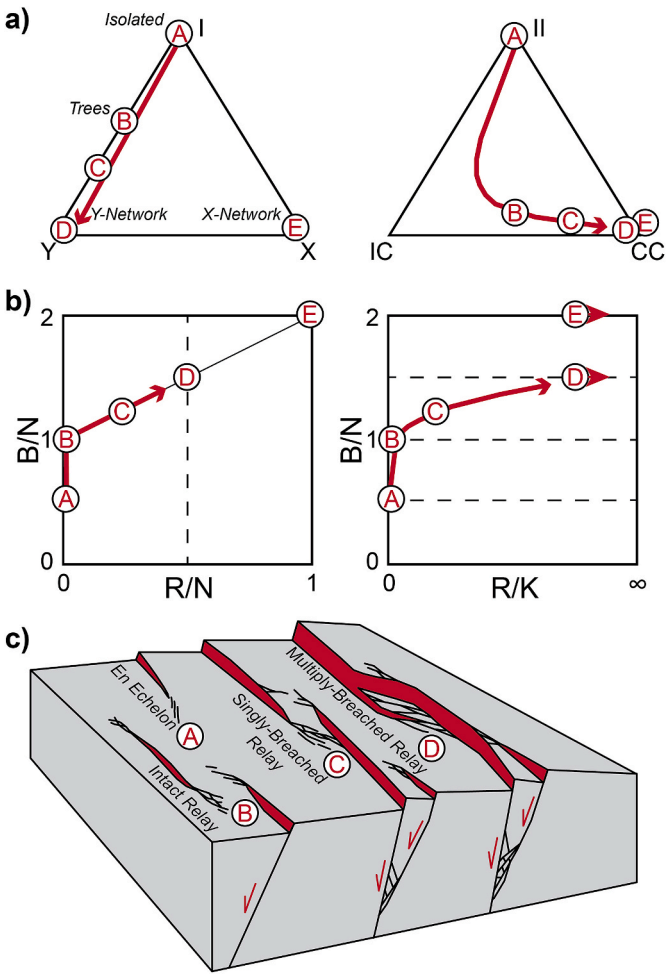

Fig. 13. Schematic diagram illustrating the topological and graph characteristics of fault damage zones. a) Node (left) and branch (right) triangles. b) Plots of different graph metrics with the ratio of branches to nodes (B/N) plotted against the ratio of regions to nodes (R/N) and the ratio of regions to components (R/K) on the left and right, respectively. Positions A to E represent fracture networks with different topological and graph characteristics. The red arrows illustrate potential topological pathways for an evolving damage zone, as illustrated by the block diagram in c).

fractures splay from or abut the ENE-trending relay bounding faults (i.e. CS8 to CS9 and CS11 to CS12; Fig. 11b and d). The highest connecting frequencies (>2000 N_c/m^2) also occur along the relay breach (i.e. CS8-CS12), with a major bullseye and maximum profile peak in sample CS11 where breaching fractures splay and abut the southern relay bounding fault (Fig. 11c and e). Minor bullseyes and peaks in connecting node frequency also occur in areas of lensing along the relay bounding faults (i.e. CS3 and CS6).

The R_{22} values in example K7 again show an inverse relationship with intensity and connecting node frequency and are considerably lower on average (<0.1) than example K5, indicating a moderate to high level of damage. The increased fracture abundance along with higher numbers of intersections in the breached area produce the lowest R_{22} values, tending towards 0.01 (Fig. 11g). Unlike the other parameters the average degree ($<D>$) is relatively constant along-strike of the damage zone, ranging from ~2.5 to ~3 (Fig. 11f). Slightly higher values of $<D>$ coincide with areas of lensing along the relay bounding faults and the breached relay area, matching patterns in fracture intensity and connecting node frequency.

5.4.3. Splay fault damage zone: example K3

Example K3 is a NNW-dipping normal fault observed in a cliff section

offsetting the LGLM and MGLM with a maximum throw of ~40 cm (Fig. 1b). The fault is planar in the MGLM, with a dip of ~60°, whereas in the LGLM the fault has a more listric character (Fig. 12a). Within the LGLM fracturing around the fault is dominated by long layer-parallel fractures, whereas within the MGLM there are numerous steeply dipping antithetic and synthetic faults/fractures. Key features include a lens stretching in and above a phosphoritic conglomerate at the top of the LGLM and a footwall splay zone located in the upper part of the outcrop within the MGLM (Fig. 12a).

Within the LGLM (CS1 to CS16) the splay damage zone shows relatively low fracture intensities (<50 m^{-1}; Fig. 12b and d) and connecting node frequencies (<1000 N_c/m^2; Fig. 12c and e). Furthermore, along this interval R_{22} values undulate around an average of ~0.3, a relatively low amount of damage. The transition from the LGLM through the phosphoritic conglomerate to the MGLM (CS17 to CS21) shows an increase in both fracture intensity and connecting node frequency, with peaks at CS20 immediately above the conglomerate. This spatial pattern is mirrored by the R_{22} profile, which decreases to values < 0.1 representing an increase in damage (Fig. 12g). Values of $<D>$ are highly variable within the LGLM, ranging from 1.5 to 3.5 (Fig. 12f), which contrasts with the relatively low and stable profiles of fracture intensity and connecting node frequency. The high variability in connectivity within the LGLM could be related to the numerous layer-parallel fractures obliquely cross-cutting the main fault and its subsidiary faults and fractures.

In the MGLM, discrete bullseyes and peaks in both fracture intensity (Fig. 12b and d) and connecting node frequency (Fig. 12c and e) occur where the largest antithetic fault/fracture intersects the main fault (CS22 to CS24). At this intersection point there is also a significant decrease in R_{22}, which tends towards 0.01 (Fig. 12g), indicating a high amount of damage with the rock mass very broken up at this location. The highest fracture intensities and connecting node frequencies along K3 occur within the footwall splay zone (CS32 to CS37), where broad bullseyes and peaks occur immediately above the main splay bifurcation point (Fig. 12a–e). The peaks in fracture intensity and the number of connections measured in these circle samples coincide with the lowest R_{22} values (0.01; Fig. 12g), highlighting that these samples represent a highly damaged zone. Within the MGLM, highs in $<D>$ broadly coincide with highs in fracture intensity and connecting node frequency as well as lows in R_{22}. This shows that the degree of connectivity can be influenced spatially by large changes in the fracture abundance and the number of connections.

6. Discussion

6.1. New characteristics of damage zones from topology and graph metrics

The application of topology and graph metrics to damage zones adds information to their characterisation based on the underlying relationships between the fractures within their fracture networks. The node and branch topological model (Figs. 3a and 13a) describes the different types of connections between the fractures and how fracture traces are connected to others within the network (Sanderson and Nixon, 2015, 2018). In addition, graph metrics provide a generalisation of the constitutive elements (nodes, branches, regions and components) that make-up each fracture network (Figs. 3b and 13b; Sanderson et al., 2019) and how those elements relate to one another. Thus, these two approaches provide a means to classify networks based on their arrangement and connectivity, complementing traditional studies that focus on describing their architecture and geometry (e.g. McGrath and Davison, 1995; Kim et al., 2004; Choi et al., 2016; Peacock et al., 2017). Our results indicate that different types of damage zone are characterised by distinct topological signatures and graph metrics, with differences and similarities between each type (as summarised by Fig. 13):

- *Tip-damage zones (Positions A-C)* – En echelon tips have simple networks consisting of numerous isolated fractures, thus they plot between positions A and B on Fig. 13 as unconnected fracture networks (i.e. $C_B < 1.3$; Fig. 8) with high proportions of *I*-nodes and *II*-branches (Fig. 7). These networks comprise numerous components with very low branch to node ratios ($B/N < 1$) and no regions (Fig. 9). At position B, complex tip-damage zones (e.g. horsetail tips, bifurcating tips) form, producing more connected fracture networks (i.e. $C_B = 1.3$–1.6; Fig. 8) with increased proportions of *Y*-nodes and high proportions of *IC*-branches (Fig. 7). These networks begin to form numerous small tree-like components with low branch to node ratios ($B/N = 1$) and very few regions (Fig. 9).
- *Relay-damage zones (Positions B-D)* – Intact relays consist of two overlapping fault tips that are approach one another but do not link, resulting in characteristics similar to tip-damage zones, generally plotting between positions B and C on Fig. 13. Singly-breach relays plot close to C, forming complex and moderately connected networks (i.e. $C_B > 1.6$; Fig. 8) with greater proportions of *Y*-nodes and *CC*-branches (Fig. 7b). Thus, their networks produce large tree-like components with high branch to node ratios (B/N up to ~1.3) and moderate numbers of regions (Fig. 9). Finally, multiply-breached relays tend to plot closer to D, representing well-connected networks (with $C_B > 1.8$; Fig. 8) dominated by *Y*-nodes and high proportions of *CC*-branches. These consist of a few large interconnected components with very high branch:node ratios ($B/N > 1.3$) and high numbers of regions (Fig. 9).
- *Splay-damage zones (Positions C-D)* – Although these fault damage zones are observed in cross-section they show similar characteristics to singly- and multiply-breached relays, plotting between positions C and D on Fig. 13. The fracture networks display a moderate degree of connectivity (i.e. $C_B > 1.6$; Fig. 8), due to high proportions of *Y*-nodes and *CC*-branches (Fig. 7). They also produce large tree-like components with high branch to node ratios, the same as singly-breached relays, but generally have fewer components with more regions (i.e. Fig. 9).

The topological characteristics and graph metrics of the studied damage zones indicate a clear link to their structural style and complexity (i.e. high fracture abundances, range of orientations), with tip-damage zones forming the simplest networks and relay-damage zones forming the most complex. Tip-damage zones accommodate decreases in displacement at fault tips and are generated by stress concentrations, which are enhanced by larger displacement gradients (e.g. Cowie and Scholz, 1992; Cowie and Shipton, 1998; Shipton and Cowie, 2003). However, relay-damage zones involve the interacting stress fields of two fault tips, which inhibits tip propagation and increases displacement gradients as well as causes local rotations in the stress field between the two faults (c.f. Willemse et al., 1996; Crider and Pollard, 1998; Gupta and Scholz, 2000; Kattenhorn et al., 2000). Thus, the resultant damage zones will exhibit greater fracture intensities and varied fracture orientations in comparison to isolated fault tip-damage zones (e.g. Peacock and Sanderson, 1994; Bastesen and Rotevatn, 2012; Fossen and Rotevatn, 2016). Such increases in fracture intensity and variations in fracture orientation will increase connectivity (e.g. Sanderson and Nixon, 2018). Thus, more structurally complex damage zones are generally better connected, with greater proportions of connecting nodes and *CC*-branches that form larger components with more regions. Similar relationships between structural complexity and topological character have been described for rift fault networks, where complex multiphase rifts form more connected networks with higher proportions of *Y*-nodes and *CC*-branches in comparison to simple single-phase rifts (Morley and Nixon, 2016; Duffy et al., 2017).

Overall these topological and graph characteristics provide new quantitative descriptions of network arrangement and connectivity, allowing a more meaningful comparison of the different damage zone types. An additional advantage of using topology and graph theory is that they are dimensionless and therefore the topology of damage zones and their fracture networks can be used and compared on a range of scales. Furthermore, the distinct topologies and trends in their graph metrics make it possible to predict the properties of the different damage zones.

This can be useful when estimating deformation around fault tips and fault linkage in the subsurface, where small-scale structures in damage zones are not easily observed due to data resolution limitations (e.g. seismic reflection data; Enge et al., 2007) Thus this can have implications when assessing fluid-flow conduits and barriers (e.g. Leveille et al., 1997), the integrity of structural traps (e.g. Gartrell et al., 2006) and the structural configuration and compartmentalization of reservoirs in large-scale fault tips and relay damage zones (e.g. Pickering et al., 1997; Rotevatn et al., 2009; Rotevatn and Fossen, 2011; Richards et al., 2015).

6.2. Damage zone development and topological pathways

When faults grow they propagate, interact and accumulate slip to increase in both length and displacement, allowing them to accommodate greater strains and become more linked (e.g. Cowie and Scholz, 1992; Peacock and Sanderson, 1994; Cartwright et al., 1995; Cowie et al., 2000; Walsh et al., 2001; Childs et al., 2003; Bull et al., 2006; Duffy et al., 2017; Rotevatn et al., 2019). During these processes of fault evolution, damage zones will generally increase in size and become more complex (Shipton and Cowie, 2001, 2003; e.g. Kim et al., 2003; Fossen et al., 2005; Childs et al., 2009; Bastesen and Rotevatn, 2012). For example, slip accumulation on a fault will enhance stress concentrations at the fault tip, producing a wider and more intense tip-damage zone (c.f. Shipton and Cowie, 2003). Furthermore, if the fault tip propagates and interacts with another fault then the tip-damage zone will evolve into a relay-damage zone, adding more damage structures to or overprinting the existing damage zone (Kim et al., 2003, 2004).

The variety of structural styles and complexities of the tip- and relay-damage zones observed in the study area illustrate this spectrum of damage zone development, as presented in the evolutionary model shown in Fig. 13c (i.e. A-D). Firstly, we infer that en echelon tips (A) might evolve into more complex horsetail and bifurcating tips (B) with increased slip and tip propagation, similar to the tip-damage zone evolution suggested by Kim et al. (2003) for strike-slip faults. Secondly, the three types of relay-damage zone clearly represent different stages of fault linkage (e.g. Peacock and Sanderson, 1991, 1994; Walsh and Watterson, 1991; Huggins et al., 1995; Childs et al., 2009; Bastesen and Rotevatn, 2012; Fossen and Rotevatn, 2016), with intact relays (B) expected to evolve into singly-breached relays (C) and finally multiply-breached relays (D) as the faults progressively interact and link. Using this evolutionary model, we discuss how the topology and graph characteristics of the damage zones might develop and how their arrangement and connectivity potentially evolves.

The topological and graph characteristics of the tip- and relay-damage zones (Figs. 7 and 9) indicate that they evolve along well-constrained topological pathways, as illustrated by the red arrows between positions A and D on Fig. 13a and b. The tip-damage zones only evolve part way along these pathways, initially dominated by I-nodes and II-branches before forming more *Y*-nodes and *IC*-branches and eventually *CC*-branches (Fig. 13a). This represents fractures splaying and bifurcating as horsetail/bifurcating tip-damage zones develop. The node to branch ratios of the damage zones increase (particularly between positions A and B) as components increase in size and begin to link to form trees. After position B the components are connected enough to start forming regions (Fig. 13b).

Relay-damage zones evolve further along the topological pathways, becoming dominated by *Y*-nodes and *CC*-branches (Fig. 13b; positions B-D) as across-fault fractures develop within the relay and abut/cross-cut each other. Once the relays start to breach at position C, the number of components decreases as the two tip-damage zones of the interacting faults link to form larger interconnected networks. The number of regions per component substantially increases as more and more regions form within these interconnected damage zones.

These topological pathways provide important insights into how networks develop in damage zones during fault evolution. The node and branch topologies evolve along similar pathways predicted for rift fault networks as shown by Duffy et al. (2017). They apply node and branch topology to physical clay analogue models, showing how topology changes in fault networks with increasing finite strain. Their results are compared with natural examples of rift fault networks and also highlight the importance of across-strike faulting in reaching more evolved topologies. The similarities between the damage zone fracture networks and rift fault networks suggest that the pathways highlighted in this study could be more widely applied to larger scale fault networks.

6.3. Controls on spatial variability along fault damage zones

All the studied damage zones show spatial variability in their complexity along-strike/dip. More simple zones consist of a fault segment and damage with low fracture intensities and connecting node frequencies, which leave the rock mass relatively intact. These separate more complex parts consist of higher fracture intensities and connecting node frequencies that break up the rock mass into numerous blocks. These complex zones are often located around irregularities along the faults/fractures, such as bends that create lenses or intersections associated with bifurcations/abutments. As faults accrue displacement, these irregularities can locally perturb or concentrate stress, enhancing the development of fractures within the damage zone (e.g. Segall and Pollard, 1980; Rawnsley et al., 1992; Willemse and Pollard, 1998; Maerten et al., 2002; Berg and Skar, 2005; Fossen et al., 2005; Childs et al., 2009).

The fault splay-damage zones also show variations in damage between the different limestone members observed in the study area. In the Lower Globergerina Limestone Member (LGLM) a simple damage zone is observed, whereas in the Middle Globergerina Limestone Member (MGLM) more complex zones develop around intersections with splay faults and numerous antithetic faults. Studies have shown how changes in the mechanical and compositional properties of limestones can affect fracturing and faulting (e.g. Wennberg et al., 2006; Ortega et al., 2010; Michie et al., 2014; Korneva et al., 2018). Ortega et al. (2010) and Korneva et al. (2018) highlight how the level of dolomitization can control fracture intensity, but the limestones in the study area do not appear dolomitized. Wennberg et al. (2006) and Michie et al. (2014) illustrate the influence of texture and grainsize on fracturing and fault zone development, respectively. Both indicate that more fine-grained mud-supported limestones are likely to develop more fractures and large fracture networks than more coarse-grained, grain-supported limestones. As the MGLM consists of mudstones and the LGLM is composed of packstones and wackestones (Pedley et al., 1976; Pedley, 1987), we suggest the difference in damage zone development is caused by contrasts in grain size and mud composition of the limestones. This highlights the importance of considering the lithology when considering the character of damage zones and fault related deformation.

The presence of structurally complex zones highlights that deformation is not evenly distributed within a damage zone. It has been shown that such zones of increased fracturing and complexity can accommodate greater strains within the damage zone and help maintain strain compatibility (Nixon et al., 2019). Furthermore, such zones of complexity can have an impact on the behaviour of fluids within a damage zone. If the fractures are open, then these zones of high fracture abundance can enhance and localise flow (e.g. Davatzes et al., 2003; Kim and Sanderson, 2010; Dimmen et al., 2017, 2020). The variety in fracture orientations and the increased number of intersections helps maintain flow pathways, due to a greater probability that fractures are optimally orientated to remain open in any given stress-field (Sanderson and Zhang, 2004). Thus, in tight carbonate rocks with low matrix permeability the structurally complex zones can represent highly-permeable conduits for fluid flow (e.g. Tamagawa and Pollard, 2008; Rotevatn and Bastesen, 2014).

6.4. Insights into the three-dimensional connectivity of faults tips and relay zones

Traditionally many of the descriptions of fault tip- and relay-damage zones have been acquired from two-dimensional outcrop surfaces (e.g. McGrath and Davison, 1995; Kim et al., 2003; Peacock et al., 2017; Nixon

et al., 2019; this study), and there have been less observations of their three-dimensional character. Multiple sections through a fracture network can be used for providing more representative measurements of the network in three-dimensions – for example, one could apply stereology and average results from the different sections (e.g. Sanderson et al., 2019). The splay-damage zones in this study represent cross sections through either a relay- or tip-damage zone, providing an opportunity to compare their plan-view and cross-sectional characteristics in topology and connectivity. In plan-view there is much variability in topology (i.e. Fig. 7) and connectivity (i.e. Fig. 8) of the different tip- (i.e. C_B = ~0.5 to ~1.6) and relay-damage zones (i.e. C_B = ~1.2 to ~1.9). In contrast, the splay-damage zones produce more consistent topologies and connectivity (i.e. C_B = ~1.65 to ~1.8), despite variations in style and complexity (i.e. Figs. 7 and 8). This suggests that even if fractures are not well connected along-strike (i.e. $C_B <$ 1.5; Sanderson and Nixon, 2015, 2018), it is likely that they are connected along-dip in cross-section (i.e. $C_B > 1.5$; Sanderson and Nixon, 2015, 2018). This is due to the formation of both synthetic and antithetic fractures within the damage zones and their opposing dip directions (i.e. Fig. 6). In low-permeability carbonate rocks, where the fractures provide permeability, such variations in fracture connectivity increases the potential for anisotropy in the rocks permeability (e.g. Balberg and Binenbaum, 1983; Long and Witherspoon, 1985; Zhang and Sanderson, 1995) as it impacts the percolation threshold of the fracture network (e.g. Manzocchi, 2002; Saevik and Nixon, 2017; Sanderson and Nixon, 2018). For example, if the fractures act as fluid conduits then tip-damage zones are likely to have greater along-dip permeabilities due to their low along-strike (i.e. plan view) connectivity, whereas singly-breached and multiply-breached relays are likely to have a more isotropic permeability as the degree of connectivity is similar in both sections of observation.

7. Conclusion

Field-examples of different tip-, relay- and splay-damage zones, associated with small-scale normal faults in carbonate rocks from Malta, have been mapped in detail and analysed in terms of their geometry, topology and graph characteristics. This has allowed us to document and quantify the arrangement and connectivity of the damage zone fracture networks and how they vary spatially. In addition, placing the damage zones in the context of a fault evolutionary model has allowed us to explore the potential network development of fault damage zones. Key findings include:

- Different tip-, relay- and splay-damage zones show distinct topological and graph characteristics, which are closely related to the structural style and complexity of the damage zones.
- Tip-damage zones produce the simplest networks with higher proportions of *I*-nodes and *II-/IC*-branches, resulting in low to moderate degrees of connectivity (i.e. C_B = ~0.5 to ~1.6). Their networks include many isolated and small tree-like components that have few regions.
- Relay- and splay-damage zones produce more complex networks with higher proportions of *Y*-nodes and *CC*-branches, with moderate to high degrees of connectivity (i.e. C_B = ~1.2 to ~1.9). Their networks include large tree-like or interconnected components with the potential to develop numerous regions.
- Combining information from plan-view (tip- and relay-damage zones) and cross-section (splay-damage zones) examples can provide a more representative pseudo 3-D evaluation of a damage zones topology and connectivity. Connectivity can vary considerably in plan-view but is more consistent in cross-section, which can be important for assessing permeability anisotropy.
- Locations of stress perturbations and concentrations (i.e. fault bends and fault intersection points) produce complex zones within each damage zone. These consist of higher fracture intensities and higher connecting node frequencies. Thus these complex zones exhibit greater amounts of damage, breaking the rock mass up into numerous blocks.
- As faults propagate, interact and accumulate slip their damage zones evolve along well constrained topological pathways. Networks are initially dominated by *I*-nodes and *II*-branches and evolve towards networks dominated by *Y*-nodes and *CC*-branches. Thus damage zone connectivity increases substantially as more and more fractures form in the damage zone. The components within the network will grow and link, evolving from many tree-like components to a few large interconnected components. In addition, the regions per component significantly increases as more regions form and components link.

The application of topology and graph theory to these different damage zones provides new information that complements traditional characterisations based on descriptions of their geometry and architecture. Furthermore, the topological and graph characterisation provides an important link to the fluid-flow behaviour of the damage zones by quantifying the arrangement and connectivity of their fracture networks. The distinct characteristics of the different damage zones in this study could provide useful insights when assessing flow properties of identified damage zones in the subsurface.

CRediT authorship contribution statement

Casey W. Nixon: Writing - original draft, Formal analysis, Data curation, led the writing with input, All authors contributed to the collection and analysis of data, KN led the writing with input, All authors contributed to the collection and analysis of data. **Kari Nærland:** Writing - original draft, Formal analysis, Data curation, led the writing with input, All authors contributed to the collection and analysis of data. **Atle Rotevatn:** Formal analysis, Data curation, also helped with figures, All authors contributed to the collection and analysis of data. **Vilde Dimmen:** Writing - original draft, Formal analysis, Data curation, led the writing with input, All authors contributed to the collection and analysis of data. **David J. Sanderson:** Formal analysis, Data curation, All authors contributed to the collection and analysis of data.

Declaration of competing interest

The authors declare that they have no known competing financial interests or personal relationships that could have appeared to influence the work reported in this paper.

Acknowledgements

This research was funded by a VISTA scholarship (Project Number: 6257) – a basic research program in collaboration between The Norwegian Academy of Science and Letters, and Statoil (now Equinor). Sanderson acknowledges support from a Leverhulme Emeritus Fellowship. David Peacock is thanked for useful discussions.

References

Adler, P.M., Thovert, J.F., 1999. Fractures and Fracture Networks. Kluwer Academic Publishers, Dordrecht.

Balberg, I., Binenbaum, N., 1983. Computer study of the percolation threshold in a two-dimensional anisotropic system of conducting sticks. Phys. Rev. B 28, 3799–3812. https://doi.org/10.1103/PhysRevB.28.3799.

Bastesen, E., Rotevatn, A., 2012. Evolution and structural style of relay zones in layered limestone-shale sequences: insights from the Hammam Faraun Fault Block, Suez rift, Egypt. J. Geol. Soc. 169, 477–488. https://doi.org/10.1144/0016-76492011-100.

Beach, A., Welbon, A.I., Brockbank, P.J., McCallum, J.E., 1999. Reservoir damage around faults; outcrop examples from the Suez Rift. Petrol. Geosci. 5, 109–116. https://doi.org/10.1144/petgeo.5.2.109.

Bennett, S., 1979. A Transgressive Carbonate Sequence Spanning the Paleogene Neogene Boundary on the Maltese Islands. Annales Geologiques Des Pays Helleniques, pp. 71–80.

Berg, S.S., Skar, T., 2005. Controls on damage zone asymmetry of a normal fault zone: outcrop analyses of a segment of the Moab fault, SE Utah. J. Struct. Geol. 27, 1803–1822. https://doi.org/10.1016/j.jsg.2005.04.012.

Bonson, C.G., Childs, C., Walsh, J.J., Schöpfer, M.P.J., Carboni, V., 2007. Geometric and kinematic controls on the internal structure of a large normal fault in massive

limestones: the Maghlaq Fault, Malta. J. Struct. Geol. 29, 336–354. https://doi.org/10.1016/j.jsg.2006.06.016.
Bosence, D.W.J., Pedley, H.M., 1982. Sedimentology and palaeoecology of a Miocene coralline algal biostrome from the Maltese Islands. Palaeogeogr. Palaeoclimatol. Palaeoecol. 38, 9–43. https://doi.org/10.1016/0031-0182(82)90062-1.
Bull, J.M., Barnes, P.M., Lamarche, G., Sanderson, D.J., Cowie, P.A., Taylor, S.K., Dix, J. K., 2006. High-resolution record of displacement accumulation on an active normal fault: implications for models of slip accumulation during repeated earthquakes. J. Struct. Geol. 28, 1146–1166. https://doi.org/10.1016/j.jsg.2006.03.006.
Caine, J.S., Evans, J.P., Forster, C.B., 1996. Fault zone architecture and permeability structure. Geology 24, 1025–1028. https://doi.org/10.1130/0091-7613(1996)024<1025:FZAAPS>2.3.CO;2.
Cartwright, J., Trudgill, B., Mansfield, C., 1995. Fault growth by segment linkage: an explanation for scatter in maximum displacement and trace length data from the Canyonlands Grabens of SE Utah. J. Struct. Geol. 17, 1319–1326.
Childs, C., Manzocchi, T., Walsh, J.J., Bonson, C.G., Nicol, A., Schöpfer, M.P.J., 2009. A geometric model of fault zone and fault rock thickness variations. J. Struct. Geol. 31, 117–127. https://doi.org/10.1016/J.JSG.2008.08.009.
Childs, C., Nicol, A., Walsh, J.J., Watterson, J., 2003. The growth and propagation of synsedimentary faults. J. Struct. Geol. 25, 633–648.
Choi, J.-H., Edwards, P., Ko, K., Kim, Y.-S., 2016. Definition and classification of fault damage zones: a review and a new methodological approach. Earth Sci. Rev. 152, 70–87. https://doi.org/10.1016/J.EARSCIREV.2015.11.006.
Choi, J.H., Jin, K., Enkhbayar, D., Davvasambuu, B., Bayasgalan, A., Kim, Y.S., 2012. Rupture propagation inferred from damage patterns, slip distribution, and segmentation of the 1957 MW 8.1 Gobi-Altay earthquake rupture along the Bogd fault, Mongolia. Journal of Geophysical Research B: Solid Earth 117. https://doi.org/10.1029/2011JB008676.
Cowie, P.A., Gupta, S., Dawers, N.H., 2000. Implications of fault array evolution for synrift depocentre development: insights from a numerical fault growth model. Basin Res. 12, 241–261.
Cowie, P.A., Scholz, C.H., 1992. Growth of faults by accumulation of seismic slip. J. Geophys. Res. 97, 11085–11095.
Cowie, P.A., Shipton, Z.K., 1998. Fault tip displacement gradients and process zone dimensions. J. Struct. Geol. 20, 983–997. https://doi.org/10.1016/S0191-8141(98)00029-7.
Crider, J.G., Pollard, D.D., 1998. Fault linkage: three-dimensional mechanical interaction between echelon normal faults. J. Geophys. Res.: Solid Earth 103, 24373–24391. https://doi.org/10.1029/98jb01353.
Curewitz, D., Karson, J.A., 1997. Structural settings of hydrothermal outflow: fracture permeability maintained by fault propagation and interaction. J. Volcanol. Geoth. Res. 79, 149–168. https://doi.org/10.1016/S0377-0273(97)00027-9.
Dart, C.J., Bosence, D.W.J., McClay, K.R., 1993. Stratigraphy and structure of the Maltese Graben system. J. Geol. Soc. 150, 1153–1166. https://doi.org/10.1144/gsjgs.150.6.1153.
Davatzes, N.C., Aydin, A., Eichhubl, P., 2003. Overprinting faulting mechanisms during the development of multiple fault sets in sandstone, Chimney Rock fault array, Utah, USA. Tectonophysics 363, 1–18. https://doi.org/10.1016/S0040-1951(02)00647-9.
Dimmen, V., Rotevatn, A., Nixon, C.W., 2020. The relationship between fluid flow, structures, and depositional architecture in sedimentary rocks: an example-based overview. Geofluids 2020, 1–19. https://doi.org/10.1155/2020/3506743. Article ID 3506743.
Dimmen, V., Rotevatn, A., Peacock, D.C.P., Nixon, C.W., Nærland, K., 2017. Quantifying structural controls on fluid flow: insights from carbonate-hosted fault damage zones on the Maltese Islands. J. Struct. Geol. 101, 43–57. https://doi.org/10.1016/J.JSG.2017.05.012.
Dockrill, B., Shipton, Z.K., 2010. Structural controls on leakage from a natural CO2 geologic storage site: central Utah. U.S.A. Journal of Structural Geology 32, 1768–1782. https://doi.org/10.1016/j.jsg.2010.01.007.
Duffy, O.B., Nixon, C.W., Bell, R.E., Jackson, C.A.L., Gawthorpe, R.L., Sanderson, D.J., Whipp, P.S., 2017. The topology of evolving rift fault networks: single-phase vs multi-phase rifts. J. Struct. Geol. 96, 192–202. https://doi.org/10.1016/J.JSG.2017.02.001.
Enge, H.D., Buckley, S.J., Rotevatn, A., Howell, J.A., 2007. From outcrop to reservoir simulation model: workflow and procedures. Geosphere 3, 469–490. https://doi.org/10.1130/GES00099.1.
Euler, L., 1758. Elementa doctrinae solidorum. Novi Commentarii Academiae Scientiarum Petropolitanae 4, 109–140.
Faulkner, D.R., Jackson, C.A.L., Lunn, R.J., Schlische, R.W., Shipton, Z.K., Wibberley, C. A.J., Withjack, M.O., 2010. A review of recent developments concerning the structure, mechanics and fluid flow properties of fault zones. J. Struct. Geol. 32, 1557–1575. https://doi.org/10.1016/j.jsg.2010.06.009.
Faulkner, D.R., Mitchell, T.M., Jensen, E., Cembrano, J., 2011. Scaling of fault damage zones with displacement and the implications for fault growth processes. J. Geophys. Res. 116, 1–11. https://doi.org/10.1029/2010JB007788.
Finetti, I., 1984. Geophysical study of the Sicily Channel rift zone. Boll. Geofis. Teor. Appl. 26, 3–28.
Fossen, H., Johansen, T.E.S., Hesthammer, J., Rotevatn, A., 2005. Fault interaction in porous sandstone and implications for reservoir management; examples from southern Utah. AAPG (Am. Assoc. Pet. Geol.) Bull. 89, 1593–1606. https://doi.org/10.1306/07290505041.
Fossen, H., Rotevatn, A., 2016. Fault linkage and relay structures in extensional settings—a review. Earth Sci. Rev. 154, 14–28. https://doi.org/10.1016/J.EARSCIREV.2015.11.014.
Gartrell, A., Bailey, W.R., Brincat, M., 2006. A new model for assessing trap integrity and oil preservation risks associated with postrift fault reactivation in the Timor Sea. AAPG (Am. Assoc. Pet. Geol.) Bull. 90, 1921–1944. https://doi.org/10.1306/06200605195.
Gartrell, A., Zhang, Y., Lisk, M., Dewhurst, D., 2004. Fault intersections as critical hydrocarbon leakage zones: integrated field study and numerical modelling of an example from the Timor Sea, Australia. Mar. Petrol. Geol. 21, 1165–1179. https://doi.org/10.1016/J.MARPETGEO.2004.08.001.
Gudmundsson, A., Simmenes, T.H., Larsen, B., Philipp, S.L., 2010. Effects of internal structure and local stresses on fracture propagation, deflection, and arrest in fault zones. J. Struct. Geol. 32, 1643–1655. https://doi.org/10.1016/j.jsg.2009.08.013.
Gupta, A., Scholz, C.H., 2000. A model of normal fault interaction based on observations and theory. J. Struct. Geol. 22, 865–879. https://doi.org/10.1016/S0191-8141(00)00011-0.
Huggins, P., Watterson, J., Walsh, J.J., Childs, C., 1995. Relay zone geometry and displacement transfer between normal faults recorded in coal-mine plans. J. Struct. Geol. 17, 1741–1755. https://doi.org/10.1016/0191-8141(95)00071-K.
Hull, J., 1988. Thickness-displacement relationships for deformation zones. J. Struct. Geol. 10, 431–435. https://doi.org/10.1016/0191-8141(88)90020-X.
Huyakorn, P.S., Lester, B.H., Faust, C.R., 1983. Finite element techniques for modeling groundwater flow in fractured aquifers. Water Resour. Res. 19, 1019–1035. https://doi.org/10.1029/WR019i004p01019.
Illies, J.H., 1981. Graben Formation — the Maltese Islands — a Case History. Developments in Geotectonics. Elsevier, pp. 151–168. https://doi.org/10.1016/B978-0-444-41956-9.50018-6.
Jing, L., Stephansson, O., 1997. Network topology and homogenization of fractured rocks. In: Jamtveit, B., Yardley, B.W. (Eds.), Fluid Flow and Transport in Rocks. Mechanisms and Effects. Chapman & Hall, Oxford, pp. 191–202.
Johansen, T.E.S., Fossen, H., 2008. Internal geometry of fault damage zones in interbedded siliciclastic sediments. Geological Society, London, Special Publications 299, 35–56. https://doi.org/10.1144/SP299.3.
Johri, M., Dunham, E.M., Zoback, M.D., Fang, Z., 2014. Predicting fault damage zones by modeling dynamic rupture propagation and comparison with field observations. J. Geophys. Res.: Solid Earth 119, 1251–1272. https://doi.org/10.1002/2013JB010335.
Jolivet, L., Faccenna, C., 2000. Mediterranean extension and the Africa-Eurasia collision. Tectonics 19, 1095–1106. https://doi.org/10.1029/2000TC900018.
Jongsma, D., van Hinte, J.E., Woodside, J.M., 1985. Geologic structure and neotectonics of the North African continental Margin south of sicily. Mar. Petrol. Geol. 2, 156–179. https://doi.org/10.1016/0264-8172(85)90005-4.
Kattenhorn, S.A., Aydin, A., Pollard, D.D., 2000. Joints at high angles to normal fault strike: an explanation using 3-D numerical models of fault-perturbed stress fields. J. Struct. Geol. 22, 1–23. https://doi.org/10.1016/S0191-8141(99)00130-3.
Kim, Y.-S., Andrews, J.R., Sanderson, D.J., 2000. Damage zones around strike-slip fault systems and strike-slip fault evolution, Crackington Haven, southwest England. Geosci. J. 4, 53–72.
Kim, Y.-S., Andrews, J.R., Sanderson, D.J., 2001. Reactivated strike–slip faults: examples from north Cornwall, UK. Tectonophysics 340, 173–194. https://doi.org/10.1016/S0040-1951(01)00146-9.
Kim, Y.-S., Peacock, D.C.P., Sanderson, D.J., 2004. Fault damage zones. J. Struct. Geol. 26, 503–517. https://doi.org/10.1016/j.jsg.2003.08.002.
Kim, Y.-S., Peacock, D.C.P., Sanderson, D.J., 2003. Mesoscale strike-slip faults and damage zones at Marsalforn, Gozo Island, Malta. J. Struct. Geol. 25, 793–812. https://doi.org/10.1016/S0191-8141(02)00200-6.
Kim, Y.-S., Sanderson, D.J., 2010. Inferred fluid flow through fault damage zones based on the observation of stalactites in carbonate caves. J. Struct. Geol. 32, 1305–1316. https://doi.org/10.1016/j.jsg.2009.04.017.
Kim, Y.S., Sanderson, D.J., 2008. Earthquake and fault propagation, displacement and damage zones. Structural Geology: New Research 99–118.
King, G., 1986. Speculations on the geometry of the initiation and termination processes of earthquake rupture and its relation to morphology and geological structure. Pure Appl. Geophys. 124, 567–585.
Knott, S.D., Beach, Alastair, Brockbank, P.J., Lawson, J., Mccallum, J.E., Welbon, A.I., Beach, Alastalr, Square, R.E., Glasgow, G., 1996. Spatial and mechanical controls on normal fault populations. J. Struct. Geol. 18, 359–372.
Korneva, I., Bastesen, E., Corlett, H., Eker, A., Hirani, J., Hollis, C., Gawthorpe, R.L., Rotevatn, A., Taylor, R., 2018. The effects of dolomitization on petrophysical properties and fracture distribution within rift-related carbonates (Hammam Faraun Fault Block, Suez Rift, Egypt). J. Struct. Geol. 108, 108–120. https://doi.org/10.1016/j.jsg.2017.06.005.
Leckenby, R.J., Sanderson, D.J., Lonergan, L., 2005. Estimating flow heterogeneity in natural fracture systems. J. Volcanol. Geoth. Res. 148, 116–129. https://doi.org/10.1016/j.jvolgeores.2005.03.017.
Leveille, G., Knipe, R., More, C., Ellis, D., Dudley, G., Jones, G., Fisher, Q.J., Allinson, G., 1997. Compartmentalization of Rotliegendes Gas Reservoirs by Sealing Faults, Jupiter Fields Area, Southern North Sea, vol. 123. Geological Society, London, Special Publications, pp. 87–104.
Long, J.C.S., Witherspoon, P.A., 1985. The relationship of the degree of interconnection to permeability in fracture networks. J. Geophys. Res. 90, 3087. https://doi.org/10.1029/JB090iB04p03087.
Maerten, L., Gillespie, P., Pollard, D.D., 2002. Effects of local stress perturbation on secondary fault development. J. Struct. Geol. 24, 145–153. https://doi.org/10.1016/S0191-8141(01)00054-2.
Manzocchi, T., 2002. The connectivity of two-dimensional networks of spatially correlated fractures. Water Resour. Res. 38, 1162. https://doi.org/10.1029/2000WR000180.

Mauldon, M., Dunne, W.M., Rohrbaugh, M.B., 2001. Circular scanlines and circular windows: new tools for characterizing the geometry of fracture traces. J. Struct. Geol. 23, 247–258. https://doi.org/10.1016/S0191-8141(00)00094-8.
McGrath, A., Davison, I., 1995. Damage zone geometry around fault tips. J. Struct. Geol. 17, 1011–1024.
Micarelli, L., Moretti, I., Daniel, J.M., 2003. Structural properties of rift-related normal faults: the case study of the Gulf of Corinth, Greece. J. Geodyn. 36, 275–303. https://doi.org/10.1016/S0264-3707(03)00051-6.
Micarelli, L., Moretti, I., Jaubert, M., Moulouel, H., 2006. Fracture analysis in the south-western Corinth rift (Greece) and implications on fault hydraulic behavior. Tectonophysics 426, 31–59. https://doi.org/10.1016/j.tecto.2006.02.022.
Michie, E.A.H., Haines, T.J., Healy, D., Neilson, J.E., Timms, N.E., Wibberley, C.A.J., 2014. Influence of carbonate facies on fault zone architecture. J. Struct. Geol. 65, 82–99. https://doi.org/10.1016/j.jsg.2014.04.007.
Mitchell, T.M., Faulkner, D.R., 2012. Towards quantifying the matrix permeability of fault damage zones in low porosity rocks. Earth Planet Sci. Lett. 339–340, 24–31. https://doi.org/10.1016/j.epsl.2012.05.014.
Mitchell, T.M., Faulkner, D.R., 2009. The nature and origin of off-fault damage surrounding strike-slip fault zones with a wide range of displacements: a field study from the Atacama fault system, northern Chile. J. Struct. Geol. 31, 802–816. https://doi.org/10.1016/j.jsg.2009.05.002.
Morley, C.K., Nixon, C.W., 2016. Topological characteristics of simple and complex normal fault networks. J. Struct. Geol. 84, 68–84. https://doi.org/10.1016/j.jsg.2016.01.005.
Nærland, K., 2016. Topology of Normal Fault Damage Zones in Carbonate Rocks, Malta-implications for the Development of Connectivity in Evolving Fault Networks. MSc. thesis. Department of Earth Science. University of Bergen, unpublished.
Nixon, C.W., Sanderson, D.J., Bull, J.M., 2012. Analysis of a strike-slip fault network using high resolution multibeam bathymetry, offshore NW Devon U.K. Tectonophysics 541–543, 69–80. https://doi.org/10.1016/j.tecto.2012.03.021.
Nixon, C.W., Vaagan, S., Sanderson, D.J., Gawthorpe, R.L., 2019. Spatial distribution of damage and strain within a normal fault relay at Kilve, U.K. J. Struct. Geol. 118, 194–209. https://doi.org/10.1016/J.JSG.2018.10.016.
Nyberg, B., Nixon, C.W., Sanderson, D.J., 2018. NetworkGT: a GIS tool for geometric and topological analysis of two-dimensional fracture networks. Geosphere 14, 1618–1634. https://doi.org/10.1130/GES01595.1.
Ogata, K., Senger, K., Braathen, A., Tveranger, J., 2014. Fracture corridors as seal-bypass systems in siliciclastic reservoir-cap rock successions: field-based insights from the Jurassic Entrada Formation (SE Utah, USA). J. Struct. Geol. 66, 162–187. https://doi.org/10.1016/j.jsg.2014.05.005.
Ortega, O.J., Gale, J.F.W., Marrett, R., 2010. Quantifying diagenetic and stratigraphic controls on fracture intensity in platform carbonates: an example from the Sierra Madre Oriental, northeast Mexico. J. Struct. Geol. 32, 1943–1959. https://doi.org/10.1016/J.JSG.2010.07.004.
Peacock, D.C.P., Dimmen, V., Rotevatn, A., Sanderson, D.J., 2017. A broader classification of damage zones. J. Struct. Geol. 102, 179–192. https://doi.org/10.1016/J.JSG.2017.08.004.
Peacock, D.C.P., Sanderson, D.J., 1994. Geometry and development of relay ramps in normal fault systems. AAPG (Am. Assoc. Pet. Geol.) Bull. 78, 147–165.
Peacock, D.C.P., Sanderson, D.J., 1991. Displacements, segment linkage and relay ramps in normal fault zones. J. Struct. Geol. 13, 721–733. https://doi.org/10.1016/0191-8141(91)90033-F.
Pedley, H., 1987. Controls on Cenozoic carbonate deposition in the Maltese Islands: review and reinterpretation. Memor. Soc. Geol. Ital. 38, 81–94.
Pedley, H.M., House, M.R., Waugh, B., 1976. The geology of Malta and Gozo. PGA (Proc. Geol. Assoc.) 87, 325–341. https://doi.org/10.1016/S0016-7878(76)80005-3.
Perrin, C., Manighetti, I., Ampuero, J.P., Cappa, F., Gaudemer, Y., 2016. Location of largest earthquake slip and fast rupture controlled by along-strike change in fault structural maturity due to fault growth. J. Geophys. Res.: Solid Earth 121, 3666–3685. https://doi.org/10.1002/2015JB012671.
Pickering, G., Peacock, D.C.P., Sanderson, D.J., Bull, J.M., 1997. Modeling tip zones to predict the throw and length characteristics of faults. AAPG (Am. Assoc. Pet. Geol.) Bull. 81, 82–99.
Putz-Perrier, M.W., Sanderson, D.J., 2010. Distribution of faults and extensional strain in fractured carbonates of the North Malta Graben. AAPG (Am. Assoc. Pet. Geol.) Bull. 94, 435–456. https://doi.org/10.1306/08260909063.
Rawnsley, K.D., Rives, T., Petti, J.P., Hencher, S.R., Lumsden, A.C., 1992. Joint development in perturbed stress fields near faults. J. Struct. Geol. 14, 939–951. https://doi.org/10.1016/0191-8141(92)90025-R.
Reuther, C.D., Eisbacher, G.H., 1985. Pantelleria Rift - crustal extension in a convergent intraplate setting. Geol. Rundsch. 74, 585–597. https://doi.org/10.1007/BF01821214.
Richards, F.L., Richardson, N.J., Bond, C.E., Cowgill, M., 2015. Interpretational variability of structural traps: implications for exploration risk and volume uncertainty. Geological Society, London, Special Publications 421, 7–27. https://doi.org/10.1144/SP421.13.
Rotevatn, A., Bastesen, E., 2014. Fault linkage and damage zone architecture in tight carbonate rocks in the Suez Rift (Egypt): implications for permeability structure along segmented normal faults. Geological Society, London, Special Publications 374, 79–95. https://doi.org/10.1144/SP374.12.
Rotevatn, A., Fossen, H., 2011. Simulating the effect of subseismic fault tails and process zones in a siliciclastic reservoir analogue: implications for aquifer support and trap definition. Mar. Petrol. Geol. 28, 1648–1662. https://doi.org/10.1016/j.marpetgeo.2011.07.005.
Rotevatn, A., Fossen, H., Hesthammer, J., Aas, T.E., Howell, J.A., 2007. Are relay ramps conduits for fluid flow? Structural analysis of a relay ramp in Arches National Park, Utah. Geological Society, London, Special Publications 270, 55–71. https://doi.org/10.1144/GSL.SP.2007.270.01.04.
Rotevatn, A., Jackson, C.A.L., Tvedt, A.B.M., Bell, R.E., Blækkan, I., 2019. How do normal faults grow? J. Struct. Geol. 125, 174–184. https://doi.org/10.1016/j.jsg.2018.08.005.
Rotevatn, A., Thorsheim, E., Bastesen, E., Fossmark, H.S.S., Torabi, A., Sælen, G., 2016. Sequential growth of deformation bands in carbonate grainstones in the hangingwall of an active growth fault: implications for deformation mechanisms in different tectonic regimes. J. Struct. Geol. 90, 27–47. https://doi.org/10.1016/j.jsg.2016.07.003.
Rotevatn, A., Tveranger, J., Howell, J.A., Fossen, H., 2009. Dynamic investigation of the effect of a relay ramp on simulated fluid flow: geocellular modelling of the Delicate Arch Ramp, Utah. Petrol. Geosci. 15, 45–58. https://doi.org/10.1144/1354-079309-779.
Saevik, P.N., Nixon, C.W., 2017. Inclusion of topological measurements into Analytic estimates of effective permeability in fractured Media. Water Resour. Res. 53, 9424–9443. https://doi.org/10.1002/2017WR020943.
Sanderson, D.J., Nixon, C.W., 2018. Topology, connectivity and percolation in fracture networks. J. Struct. Geol. 115, 167–177. https://doi.org/10.1016/J.JSG.2018.07.011.
Sanderson, D.J., Nixon, C.W., 2015. The use of topology in fracture network characterization. J. Struct. Geol. 72, 55–66.
Sanderson, D.J., Peacock, D.C.P., Nixon, C.W., Rotevatn, A., 2019. Graph theory and the analysis of fracture networks. J. Struct. Geol. 125, 155–165. https://doi.org/10.1016/j.jsg.2018.04.011.
Sanderson, D.J., Zhang, X., 2004. Stress-controlled localization of deformation and fluid flow in fractured rocks. Geological Society, London, Special Publications 231, 299–314.
Savage, H.M., Brodsky, E.E., 2011. Collateral damage: evolution with displacement of fracture distribution and secondary fault strands in fault damage zones. J. Geophys. Res. 116, B03405. https://doi.org/10.1029/2010JB007665.
Segall, P., Pollard, D.D., 1980. Mechanics of discontinuous faults. J. Geophys. Res.: Solid Earth 85, 4337–4350. https://doi.org/10.1029/JB085IB08P04337.
Shipton, Z.K., Cowie, P.A., 2003. A conceptual model for the origin of fault damage zone structures in high-porosity sandstone. J. Struct. Geol. 25, 333–344. https://doi.org/10.1016/S0191-8141(02)00037-8.
Shipton, Z.K., Cowie, P.A., 2001. Damage zone and slip-surface evolution over μm to km scales in high-porosity Navajo sandstone, Utah. J. Struct. Geol. 23, 1825–1844. https://doi.org/10.1016/S0191-8141(01)00035-9.
Shipton, Z.K., Evans, J.P., Kirschner, D., Kolesar, P.T., Williams, A.P., Heath, J., 2004. Analysis of CO2 leakage through "low-permeability" faults from natural reservoirs in the Colorado Plateau, east-central Utah. Geological Society, London, Special Publication 233, 43–58. https://doi.org/10.1144/GSL.SP.2004.233.01.05.
Shipton, Z.K., Evans, J.P., Robeson, K.R., Forster, C.B., Snelgrove, S., 2002. Structural heterogeneity and permeability in faulted eolian sandstone: implications for subsurface modeling of faults. AAPG (Am. Assoc. Pet. Geol.) Bull. 86, 863–883. https://doi.org/10.1306/61eedbc0-173e-11d7-8645000102c1865d.
Sibson, R.H., 1989. Earthquake faulting as a structural process. J. Struct. Geol. 11, 1–14. https://doi.org/10.1016/0191-8141(89)90032-1.
Soliva, R., Benedicto, A., Schultz, R.A., Maerten, L., Micarelli, L., 2008. Displacement and interaction of normal fault segments branched at depth: implications for fault growth and potential earthquake rupture size. J. Struct. Geol. 30, 1288–1299. https://doi.org/10.1016/j.jsg.2008.07.005.
Tamagawa, T., Pollard, D.D., 2008. Fracture permeability created by perturbed stress fields around active faults in a fractured basement reservoir. AAPG (Am. Assoc. Pet. Geol.) Bull. 92, 743–764. https://doi.org/10.1306/02050807013.
Vermilye, J.M., Scholz, C.H., 1998. The process zone: a microstructural view of fault growth. J. Geophys. Res.: Solid Earth 103, 12223–12237. https://doi.org/10.1029/98JB00957.
Walsh, J.J., Childs, C., Meyer, V., Manzocchi, T., Imber, J., Nicol, A., Tuckwell, G., Bailey, W.R., Bonson, C.G., Watterson, J., Nell, P.A., Strand, J., 2001. Geometric controls on the evolution of normal fault systems. Geological Society, London, Special Publications 186, 157–170. https://doi.org/10.1144/GSL.SP.2001.186.01.10.
Walsh, J.J., Watterson, J., 1991. Geometric and kinematic coherence and scale effects in normal fault systems. In: Roberts, A.M., Yielding, G., Freeman, B. (Eds.), Geological Society, vol. 59. Special Publications, London, pp. 193–203.
Wennberg, O.P., Svana, T., Azizzadeh, M., Aqrawi, A.M.M., Brockbank, P., Lyslo, K.B., Ogilvie, S., 2006. Fracture intensity vs. mechanical stratigraphy in platform top carbonates: the Aquitanian of the Asmari formation, Khaviz anticline, Zagros, SW Iran. Petrol. Geosci. 12, 235–246. https://doi.org/10.1144/1354-079305-675.
Willemse, E.J.M., Pollard, D.D., 1998. On the orientation and patterns of wing cracks and solution surfaces at the tips of a sliding flaw or fault. J. Geophys. Res.: Solid Earth 103, 2427–2438. https://doi.org/10.1029/97jb01587.
Willemse, E.J.M., Pollard, D.D., Aydin, A., 1996. Three-dimensional analyses of slip distributions on normal fault arrays with consequences for fault scaling. J. Struct. Geol. 18, 295–309. https://doi.org/10.1016/S0191-8141(96)80051-4.
Zhang, X., Sanderson, D.J., 1995. Anisotropic features of geometry and permeability in fractured rock masses. Eng. Geol. 40, 65–75. https://doi.org/10.1016/0013-7952(95)00040-2.